university of
groningen

BACHELOR THESIS

Long-lived activation products around the AGOR cyclotron at PARTREC

Author:
Dirk Weistra,
S3739775

Supervisor/First examiner:
Emiel van der Graaf
Second examiner:
Peter Dendooven

For the bachelor degree program of Physics
Medical Physics Group,
Department of Radiation Oncology,
University Medical Centre Groningen.

July 2, 2021

Abstract

The goal of the work presented in this thesis was to investigate the induced activity in one of the irradiation cells vaults (H-cell) at the PARticle Therapy REsearch Center of long-lived nuclides in air using theory; in dust using a HPGe detector; and in the carbon beam stop and breadboard using a small Kromek GR1 CZT detector. Furthermore, the activity of two large magnets originating from the downstream part of the TRIµP beam line was investigated using the Kromek detector. For air it was determined that an activity due to ^{7}Be of 550 Bq/nAh is produced in a 3.5 m column of air for protons with energies higher than 100 MeV. Furthermore, it was determined that the carbon beam stop can be modelled as having an active cylinder with a homogeneous ^{7}Be distribution, which (at time of measurement) had an activity 22(8) Bq/g. It was then established that for future experiments a single measurement with the Kromek GR1 CZT detector can be used to determine the activity of the beam stop using an efficiency of $1.7(3) \times 10^{-4}$. Moreover, it was found that it is unlikely that the activity of ^{7}Be in dust floating around the H-cell poses any threat to personnel. In addition, on the breadboard ^{54}Mn was found with a maximum activity concentration of 1.00(6) Bq/g and ^{51}Cr with a maximum activity concentration of 0.29(4) Bq/g. Besides these, there were also some ^{60}Co traces and ^{124}Sb visible, though the latter most likely originated from the lead shielding used in the experiment. Finally, the two magnets showed no measurable activity on both the inside and outside and determination of the minimal detectable activities showed induced activity due to ^{54}Mn or ^{60}Co should be below their respective clearance values.

Acknowledgements

Contents

1 Introduction

Radiation safety is an important aspect in proton irradiation facilities such as the PARticle Therapy REsearch Center (PARTREC), a research centre linked with the UMCG Groningen Proton Therapy Center (GPTC). During irradiation in such facilities, the proton beam can interact with air or components along the beam line. This can cause the creation of radioactive reaction products[1]. The presence of these radionuclides can give a small dose to personnel or a patient undergoing radiotherapy. The aim of this thesis is to investigate the induced activity of different components around the AGOR cyclotron, which is the central infrastructure of PARTREC; more specifically, components in the H-cell, which is one of the irradiation vaults. In this thesis we only look at radionuclides which cause long term activity, which in practice means still detectable after roughly a month.

The H-cell is an irradiation vault in which the proton beam travels through air before striking a target. On average the AGOR cyclotron produces a beam of 150 MeV to 190 MeV protons with a current of 20 nA to 50 nA[2]. In the H-cell various components are placed along the beam line: collimators, degraders and a carbon beam stop for example. Figure 1 shows a schematic overview of the beam line in the H-cell with various components placed on a breadboard table.
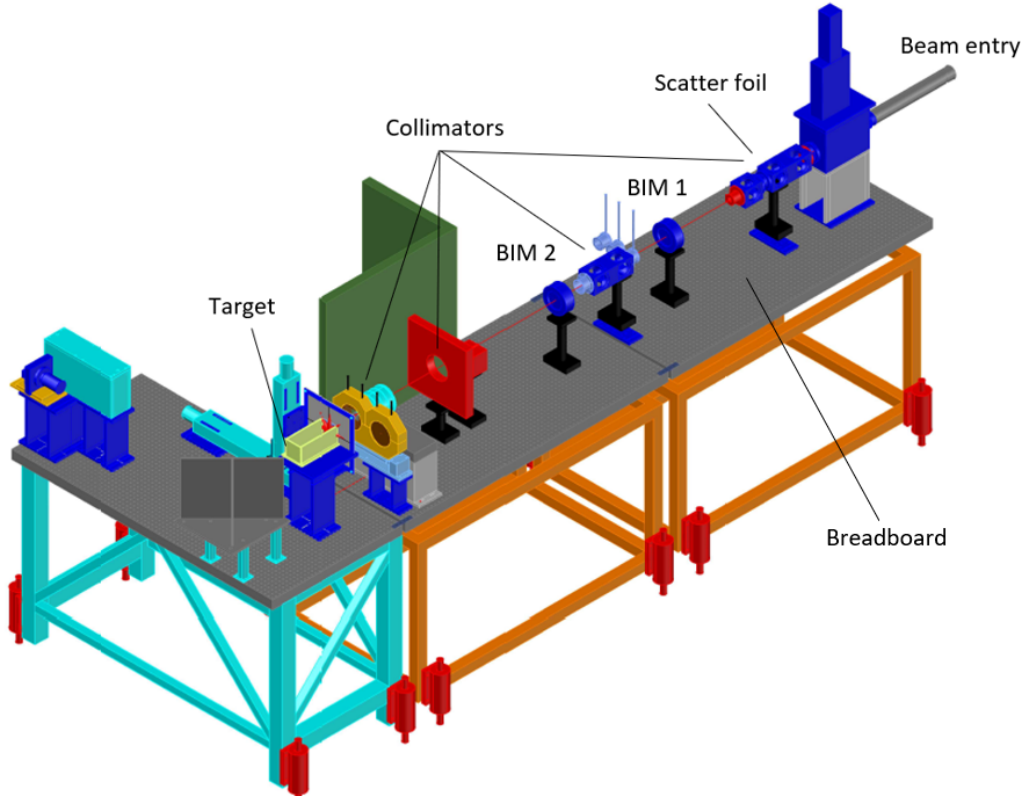
Figure 1: *Lay-out of the beam line in the H-cell. Adapted from [3].*

These components can be categorized into two categories. The first includes objects which are in direct contact with the proton beam and the second includes the objects that are not in direct contact with it. Objects of the first category can become radioactive through direct contact with the protons. Reaction products are then formed which include radioactive nuclides, but also neutrons. In turn these neutrons can also react with objects and make them radioactive. Objects of the secondary category can thus only become radioactive due to neutron interactions.

In this thesis the following potential radiation sources in the H-cell were investigated: the beam stop, air, dust and the breadboard. Besides these, two magnets originating from the downstream part of the TRIµP beam line were investigated. Before striking a target, the beam will travel through $3.5\,\mathrm{m}$ of air in which naturally some dust floats around. Both air and dust are comprised largely of low Z elements, primarily carbon (C), oxygen (O) and nitrogen (N). When a proton beam strikes such atoms, there is a probability that it creates the radioactive Beryllium-7 (^{7}Be) with a half-life of 53 days[4]. More information regarding ^{7}Be is given in the theory section since it plays a significant part throughout this thesis. Since the density of air is relatively low compared to e.g. water and solids, and the amount of dust in contact with the beam is also low, the induced activity from ^{7}Be will likely be very low as well. As it is hard to measure the ^{7}Be activity in air, cross sectional data will be used to estimate it. The produced ^{7}Be in air will likely fall down and thus become visible in the dust on, for example, the floor. Therefore, a dust sample was taken from the floor and components in the H-cell. This dust sample will be measured by using a HPGe gamma detector.

The beam stop is a carbon cylinder located at the end of the beam line. Its purpose is to stop any remaining proton after the beam has struck the target. Since the beam stop is made out of carbon it was expected that ^{7}Be would be formed in it. Compared to air, solid carbon has a much higher density. The activity in the beam stop is thus expected to be higher as well.

Originally a part of this thesis involved the stopping of $60\,\mathrm{MeV}$ protons beam in polyethylene (C_2H_4), polycarbonate ($C_{16}H_{14}O_3$) and nylon ($C_{12}H_{22}N_2O_2$) samples. In polyethylene, ^{7}Be can only be created from carbon. In polycarbonate, it could also be created from oxygen and in nylon also from nitrogen. This knowledge could then be used to determine what part of the induced ^{7}Be activity came from which element. The measured ^{7}Be activity in these samples could then be compared to what theoretically is predicted. However, due to a defect in the AGOR cyclotron this part was no longer possible. The calculations on the expected activity are still included at the end of the theory section.

The breadboard is not in direct contact with the proton beam, but various components placed on it are. These components can create neutrons which in turn can react with the steel of the breadboard which consists of iron (Fe) and chromium (Cr). For the breadboard it was expected that ^{54}Mn is created by fast neutrons reacting with iron. Furthermore, some ^{51}Cr and ^{60}Co is expected to be formed by thermal neutron absorption. The activities in the beam stop and the breadboard are measured with a small Kromek CZT detector to allow measurements without cutting the beam stop and breadboard into samples.

The two magnets were used in the TRIμP beam line. Instead of protons, various isotopes passed through these magnets. Since they were not placed around components which produce a lot of neutrons it is expected that they do not contain much radioactivity. If any, they might contain traces of radioactive copper or zinc from the copper coils or manganese and cobalt due to the iron surrounding the coils. The Kromek CZT detector was used for these measurements.

2   Theory

We start this theory section with a description of the interactions of protons with matter. From this follows the production and interaction of neutrons. We then move on to some information on relevant radionuclides and present some useful equations regarding the production and decay of these radionuclides. After that, the basic principles of gamma spectroscopy are explained. Gamma spectroscopy is a technique that is often used in this project to determine activities. Finally, some theoretical estimates of induced activity by protons in air, the polyethylene, polycarbonate and nylon targets, and the beam stop are given. The information in the following sections is based on [5] (Sections 2.1, 2.2, 2.4 and 2.6), [6] (Sections 2.1 and 2.2), [7] (Sections 2.4 and 2.5), [8] (Sections 2.6 and 2.7) and [9, 10] (Section 2.6), unless stated otherwise.

2.1   Proton interactions

Protons and other heavy charged particles can interact with matter in multiple ways, both with nuclei and electrons. Interactions with the nucleus include, for example, the elastic Rutherford scattering and the non-elastic spallation reaction where ^{7}Be is formed. However, in this section the focus lies on the coulombic interaction with atomic electrons. It is this interaction that is primarily responsible for the energy loss of protons. When a positively charged proton is in the vicinity of a negatively charged orbital electron, the electron feels an impulse due to the coulomb force. Depending on the proximity of the proton, the electron can either be excited to a higher state or leave the atom altogether, resulting in ionization of the atom. The energy needed for such a process is acquired from the kinetic energy of the proton which, as a result of this energy loss, slows down. For each collision a proton with mass M and kinetic energy E will lose a maximum energy of $4Em_e/M$, where m_e is the electron mass. This fraction is roughly equal to $1/500$ of the kinetic energy, and is thus very small. Therefore, it implies that a proton needs to interact many times before being stopped.

The rate at which protons, or other heavy charged particles, lose their energy through the coulomb interaction is described by the stopping power. It is defined as the differential energy loss of the particle within a medium divided by the corresponding differential path length [5]. Using relativistic quantum mechanics the following expression for the stopping power S (J/m), found by Bethe, can be derived:

$$S = -\frac{dE}{dx} = \frac{4\pi k_0^2 z^2 e^4 n_e}{mc^2\beta^2}\left[\ln\frac{2mc^2\beta^2}{I(1-\beta^2)} - \beta^2\right] \tag{1}$$

Where:

- z is the atomic number of the heavy particle (for a proton $z = 1$),

- $\beta = v/c$ is the proton's speed relative to the speed of light c,

- $k_0 = 1/(4\pi\epsilon_0)$ in which ϵ_0 is the permittivity constant,

- e is magnitude of the electron charge in C,

- m is the electron rest mass in kg,

- n_e is the electron number density of the medium in m^{-3} and

- I is the mean excitation energy of the medium in J.

This equation shows that the stopping power mainly depends on the electron density of the medium. This relation with electron density suggests the stopping power to be relatively small in less dense mediums such as air compared to e.g., water or solids. This equation will later be used to show that indeed, the stopping power in air is small for protons of 150 - 190 MeV. The Bethe equation also shows that at very low energies (i.e. $\beta \to 0$) the stopping power increases to a maximum and shows a sharp peak. This peak is called the Bragg peak. This very high energy deposition at a local spot is what makes protons very effective in cancer treatment (proton therapy). Due to continuously depositing their energy, protons will travel a finite distance, called their range. The range $R(T)$ of a particle with a kinetic energy T is related to the stopping power by the following equation:

$$R(T) = \int_0^T (S)^{-1} \, dE \tag{2}$$

It is relevant to emphasize the just described stopping power and range are due to the electrons. Though small, there is also a nuclear contribution. Furthermore, the Bethe equation breaks down at low (sub 1 MeV) energies. This is where corrections are necessary. The PSTAR database from NIST[11] is a database for stopping powers and ranges of protons which includes the nuclear contributions and the corrections for low energies. For that reason it is often used in this thesis.

Another reaction a proton can have is a spallation reaction. Such reactions are non-elastic nuclear reactions where a target nucleus is hit by an incident particle, resulting in fragmentation of the target nucleus into lighter product particles as is depicted in Figure 2. These product particles may be neutrons, protons or composite particles such as ^{7}Be. Spallation reactions are often induced by cosmic rays, but can also take place in the vicinity of accelerators due to high energetic protons or neutrons interacting with surrounding materials or air [12].
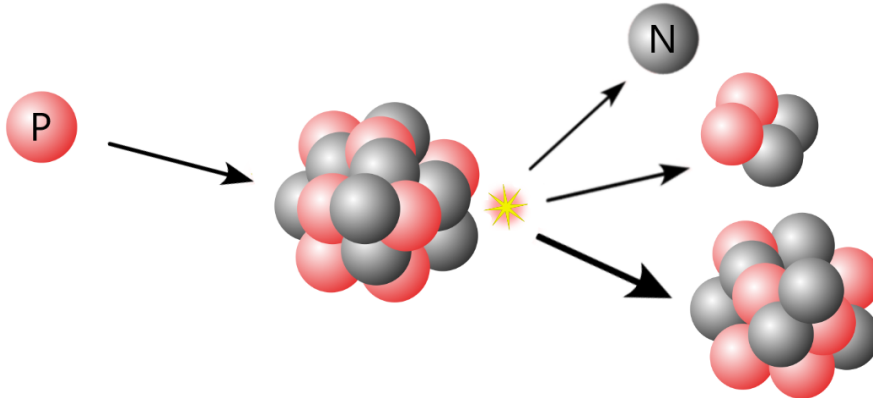
Figure 2: *An illustration of a spallation reaction: a proton strikes an atom, resulting in lighter product particles. Figure adapted from [13].*

2.2   Neutron interactions

In contrast to protons or heavy charged particles, neutrons do not carry charge. They can thus travel an appreciable distance without interacting since there is no coulomb force to slow them down. Neutrons do however, interact with nuclei. The probability of different types of reactions is very much energy dependent. As a crude simplification neutrons can be divided into certain energy classes. There are fast neutrons which have an energy roughly higher than 0.1 MeV, and thermal neutrons which have an energy of roughly 0.025 eV. Thermal neutrons follow the same energy distribution as the gas molecules surrounding them. They are therefore, related to the Maxwell-Boltzmann distribution. This hence explains their room temperature energy of roughly 0.025 eV. Finally there are some classifications between them: slow, intermediate or resonance neutrons. All these classifications and energy ranges are used loosely and tend to differ depending on the author.

Neutrons often interact via elastic or inelastic scattering with the nucleus. The latter can leave the nucleus in an excited state. Another type of interaction is neutron absorption or capture. This leads to for example a (n,p), (n,α) or (n,γ) reaction. Fast neutrons tend to be slowed down by (mostly) elastic scattering until they reach thermal energies. While slowing down, the neutron keeps scattering, but simultaneously the probability of neutron absorption increases.

Due to the proton beam reacting with various components, a large neutron flux is expected to be around an accelerator. These neutrons may cause significant induced radioactivity when absorbed by materials around the accelerator. Depending on the type of material the following radioactive elements could be found according to the book by Sullivan[14]:

- ^{63}Cu in natural copper

- Sodium in concrete

- Argon in air

- Zinc in copper

- Manganese and cobalt in iron

- Antimony in lead

- Traces of manganese, cobalt, caesium and europium in earth and concrete

- Possibly ^{186}W in natural tungsten

The next section describes which of them are relevant for this thesis.

## 2.3   Production and decay of relevant radionuclides

Some useful information is given regarding the production and decay of radionuclides relevant for this thesis. Furthermore, the energies, E, of the most important gamma rays are given with their branching ratio, f. A summary with all relevant data used in calculations in the remainder of this thesis can be found in Table 1, located at the

end of this section. For this table, the decay constant λ was calculated from the half life ($t_{1/2}$) by:

$$t_{1/2} = \frac{\ln 2}{\lambda}. \tag{3}$$

Beryllium-7

As previously mentioned, one of the expected radionuclides is ^{7}Be. ^{7}Be is an unstable isotope with a half life of $53.22(6)$ days. It can be formed by spallation reactions, primarily with nitrogen, oxygen and carbon. Cross sections for these reactions are given by the graph in Figure 3.
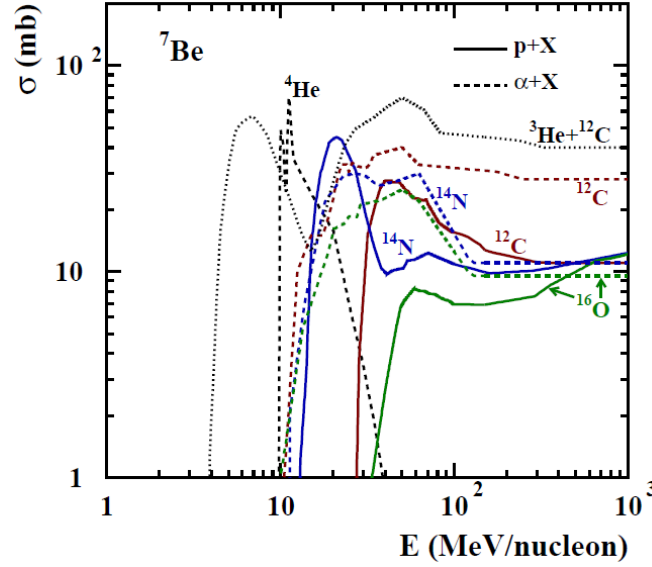
Figure 3: *Cross sections for ^{7}Be production from amongst others, protons with ^{12}C, ^{14}N and ^{16}O. Figure taken from [15]*

^{7}Be decays to ^{7}Li exclusively through electron capture; either directly to the ground state (89.56%) or via an excited state of ^{7}Li (10.44%) where a gamma ray is produced. Electron capture is a process where an orbital electron from an inner electron shell, often the K-shell, is captured by a proton. This process creates a neutron and an electron neutrino. The vacancy created by the captured electron can result into Auger electrons or characteristic x-rays. The product nucleus may be in the ground state or in an excited state so that subsequently, a gamma ray, characteristic for the product element, will be produced after nuclear de-excitation. For ^{7}Be-decay to ^{7}Li, this gamma ray has an energy of $477.621(2)$ keV [4].

Chromium-51

Since the breadboard is made of a steel alloy which contains chromium, ^{51}Cr can be expected. It can be created by neutron capture of natural chromium (^{50}Cr(n,γ)^{51}Cr) or iron (^{54}Fe(n,α)^{51}Cr). ^{51}Cr has a half life of 27.7 days which makes that it can be detected quite some time after being produced. It decays via electron capture to either the ground state of ^{51}V (90.1%) or to an excited state (9.9%) after which a 320 keV gamma ray is emitted [16].

Antimony-124

Antimony is often found in lead alloys to make it stronger[17]. Its radioactive isotope ^{124}Sb is produced by neutron capture (^{123}Sb(n,γ)^{124}Sb). ^{124}Sb can thus be found in the lead shielding bricks that are present in the H-cell and which were also used to shield the breadboard measurements. ^{124}Sb has a half life of 60.2 days and disintegrates by beta minus decay to various excited levels of ^{124}Te. The four most abundant high energy gamma rays are listed in Table 1[18].

Manganese-54

As mentioned by Sullivan[14], radioactive manganese is often found in iron targets. This is because the isotope ^{54}Mn can be created by fast neutron interactions with ^{54}Fe (^{54}Fe(n,p)^{54}Mn). It has a half life of 312 days and decays in 99.9997(3)% directly to an excited level of ^{54}Cr. After de-excitation an 835 keV gamma ray is emitted. The other decay option is a weak electron capture or beta plus transition directly to the ground state of ^{54}Cr[19].

Cobalt-60

Similar to ^{54}Mn, ^{60}Co can also be found in iron targets. It can be created through multiple stages of neutron activation of iron. Compared to the previously mentioned radionuclides, ^{60}Co has a rather long half-life of 5.3 years. It decays through beta minus decay to excited states of ^{60}Ni and eventually to its ground state by emitting gamma rays. The two most abundant gamma rays are listed in Table 1[20].

Table 1: *Properties of relevant nuclides [4, 16, 18–20]*

Element	$t_{1/2}$	λ (s^{-1})	E (keV)	f (%)
^{7}Be	53.22(6) d	$1.5074(2) \times 10^{-7}$	477.6035(20)	10.44(4)
^{51}Cr	27.7025(24) d	$2.895\,96(26) \times 10^{-7}$	320.0824(5)	9.89(2)
^{124}Sb	60.208(11) d	$1.332\,47(25) \times 10^{-7}$	602.7278(21)	97.775(22)
			645.8542(37)	10.708(22)
			722.7842(37)	7.422(15)
			1690.9842(45)	47.46(19)
^{54}Mn	312.19(3) d	$2.569\,76(25) \times 10^{-8}$	834.848(3)	99.9752(5)
^{60}Co	5.2711(8) a	$4.1671(6) \times 10^{-9}$	1173.228(3)	99.85(3)
			1332.492(4)	99.9826(6)

2.4 Nuclide production

The probability at which nuclear reactions take place is quantified by the so-called cross section σ. The cross section has dimensions of length squared, and thus units of m^2, or more common in nuclear physics, barn (b), where $1\,\text{b} = 10^{-28}$ m^2. One can think of the cross section as a fictitious effective area of the target nucleus, which must be struck by the incident particle in order for a given reaction to occur. The larger the cross section, the higher the probability of the reaction happening. The cross section depends on the type of target atom and the energy of the incoming particle.

Using the cross sections and the composition of a certain material irradiated by protons, it is possible to calculate the rate P in s^{-1} at which an element is produced in a proton beam from the equation,

$$P = \phi N \sigma x \tag{4}$$

Here N is the number density of the particles in a sample exposed to the beam, σ is the cross section and ϕ is the proton flux in particles per second. Since the cross section is energy dependent, this equation holds for a monoenergetic incident beam. For composite materials or mixtures, a summation has to be made as follows to obtain the total production rate:

$$P_T = \phi \sum_i N_i \sigma_i x \tag{5}$$

where σ_i and N_i are the cross section and number density of an element i in the composite material, respectively. It is customary to have a proton flux given as a current in nanoampere instead of number of protons per unit of time. Conversion between the two is as follows. One ampere equals one coulomb per second and one proton has a charge equal to the elementary charge of 1.602×10^{-19} C. Therefore, a current of 1 nA equals:

$$1 \, \text{nA} / 1.602 \times 10^{19} \, \text{C} = 6.24 \times 10^9 \, \text{protons/s} \tag{6}$$

2.5 Radioactive decay

During and after irradiation, the produced nuclide will immediately start to decay to (eventually) a stable atom. The rate of decay of a radionuclide is given by the following expression:

$$dN/dt = -\lambda N \tag{7}$$

where the minus sign indicates the decrease in the number of particles N. Solving Equation 7 gives the standard exponential decay function:

$$N(t) = N_0 e^{-\lambda t} \tag{8}$$

where N_0 is the number of particles of the radionuclide at $t = 0$. During irradiation, and thus production of the radionuclide, there is also some decay. To account for the simultaneous production, Equation 7 must be adjusted to include a positive production term P. The rate of change is then described by the following relation:

$$dN/dt = P - \lambda N. \tag{9}$$

The term P is the same production rate as was defined earlier in this section (see Equation 5). One should note that P, in principle, is dependent on time since during irradiation, target nuclei are lost when hit by a proton. Therefore, the number of target nuclei would decrease in time. However, the number of reactions is small compared to the available target atoms in most samples and therefore, we can assume the production rate to be independent of time. By making this assumption, above equation can easily be solved:

$$N(t) = \frac{P}{\lambda} \left(1 - e^{-\lambda t} \right). \tag{10}$$

To summarise: during irradiation the number of radionuclides is described by Equation 10 and after irradiation, it is described by Equation 8. Both these equations can

also be applied to give the activity of the radioactive sample. The activity A is defined as the number of radionuclides N multiplied by the decay constant λ:

$$A(t) = N(t)\lambda. \tag{11}$$

It describes the number of disintegrations per second and has units of becquerel (Bq). Like N it is time dependent.

2.6 Gamma spectroscopy

2.6.1 Detectors

In most of the experiments in this thesis, gamma spectroscopy is used to identify radionuclides and determine their activity. Examples of detectors used for gamma spectroscopy are gas-filled detectors, scintillation detectors and semiconductor detectors. The latter is used for this thesis and will hence be further explained. At normal conditions a semiconductor is a poor electrical conductor. However, when a gamma ray or x-ray strikes the detector material, electron-hole pairs can be produced. The electrons jump from the valence band to the conduction band. By applying a bias voltage, the charges are collected and a current is created. A useful property is that the number of electron-hole pairs, and thus also the amount of current produced, is proportional to the energy of the radiation events. A major benefit of semiconductor detectors is their high efficiency and their ability to create a relatively large current. Compared to a gas-filled detector this current is ten times larger, which allows for detection of individual radiation events, i.e. counting. These two properties are vital for the experiments performed in this thesis and hence explain why semiconductor detectors were used.

Standard semiconductor detectors are very effective for short range radiation such as alpha particles, but are not very well suited for the more penetrating gamma rays. This is caused by their limited depletion depth. This depth can be increased by lowering the concentration of impurities present in the semiconductor. Often used semiconductor materials are silicon (Si) and germanium (Ge), and it is only for the latter that a low concentration of impurities has been achieved. This resulted in the High Purity Germanium (HPGe) detector. Qualities of this detector are the high energy resolution and a high efficiency over a large range of energies. A drawback however, is the necessity to operate at low temperatures. Ge has a relatively small band gap, thus operation at room temperature can easily induce charge carriers which would produce a leakage current. Such a current is visible as noise. Cooling of the HPGe detector is achieved by using liquid nitrogen.

More recently, cadmium telluride (CdTe) and cadmium zinc telluride (CZT) have also been used for semiconductor detectors. Their major benefit is the larger band gap, which allows for near room temperature operation. The probability of photoelectric absorption per unit pathlength for CdTe is roughly 4 to 5 times higher than for Ge. CdTe is thus very well suited for applications where a small detector size is important. Compared to a HPGe detector, the energy resolution tends to be a bit smaller, especially at higher energies. It has been found that blending some ZnTe into CdTe increases the band gap at room temperature, which reduces the leakage current. Further properties of a CZT detector are similar to that of a CdTe detector. In this experiment

11

an ORTEC HPGe detector and the Kromek GR1 CZT detector are used. The latter is very small in size (1 cm cubed[21]) which makes it a very portable detector. Figure 4 shows the size difference between the two detectors used for this thesis.

Figure 4: *(a) The HPGe detector with a height of roughly* 1 m. *(b) The Kromek GR1 CZT detector with a width of* 2.5 cm*[21].*

2.6.2   Gamma-ray interactions

Since gamma-ray photons itself posses no charge, they cannot be measured directly with the just mentioned detectors. Detection is therefore dependent on photon interactions in the detector material. Depending on what interaction takes place, some or all of the photon's energy is transferred to the electron. Only in the case that all energy is transferred can anything be said on the nature of the incident gamma ray. This happens in the case of photoelectric absorption.

Photoelectric absorption is a type of interaction where the incident gamma ray transfers all its energy to a photoelectron and disappears. This photoelectron comes from the absorber atom and has an energy given by the incident photon energy, $h\nu$,[1] minus the binding energy of the electron. In a pulse-height spectrum, photoelectric absorption is visible by the full-energy peak, also called photopeak. The number of counts in this peak can be used to determine the activity as will be discussed later on. If not all the energy from the incident photon is transferred we speak of Compton scattering.

Compton scattering is a type of interaction where the gamma-ray photon is scattered and part of the energy is transferred to a recoil electron. The energy of the scattered photon $h\nu'$ in terms of its scattering angle θ is given by:

$$h\nu' = \frac{h\nu}{1 + (h\nu/m_0c^2)(1 - \cos\theta)} \tag{12}$$

Normally a range of energies over all scattering angles becomes visible in the spectrum.

---

[1] h is Planck's constant and ν is the gamma-ray frequency.

When a gamma ray has an energy larger than twice the rest mass of an electron ($2m_ec^2 = 1.022\,\mathrm{MeV}$) an interaction called pair production can occur. The incident gamma ray vanishes and an electron-positron pair is created from it. Energy exceeding that of $1.022\,\mathrm{MeV}$ is converted into kinetic energy shared by the electron and positron. The positron quickly annihilates with an electron resulting into two annihilation photons of $0.511\,\mathrm{MeV}$ each.
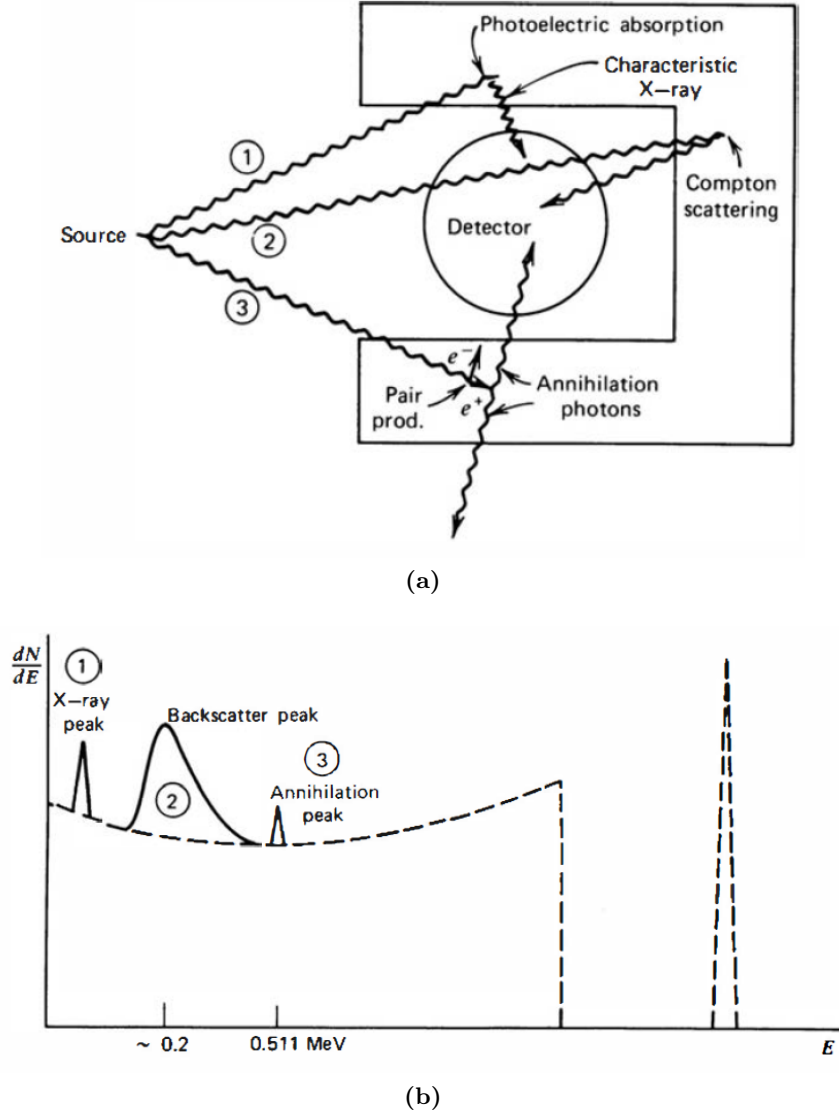
2.6.3 Pulse-height spectrum

When using a setup with a detector, amplifier and multi-channel analyser, a pulse-height spectrum can be obtained. On the horizontal axis a number of channels (often a couple of thousand) are shown, which correspond to the gamma-ray energy. The vertical axis shows the number of detected radiation events, or counts, per channel. Depending on the size of the detector, various features can be distinguished in such a spectrum. First of all, and most importantly, is the aforementioned full-energy peak corresponding to the energy of the incoming gamma ray. In the case of smaller detectors Compton interactions also play a role. Only part of the energy of the gamma ray is deposited. Since this energy depends on the scattering angle, a whole Compton continuum thus becomes visible. In the case of 180° scattering, the photon is fully backscattered and the maximum amount of energy is transferred to the electron. This energy is shown in the pulse-height spectrum as the Compton edge. For very small detectors, the corresponding spectrum is shown in Figure 5. The larger the detector becomes, the more Compton interactions can take place. This results in an area of multiple Compton events between the Compton edge and the full-energy peak. When the detector becomes infinitely large, all energy will eventually be deposited in the detector area, which results in only a full-energy peak. For large energies ($> 2m_ec^2 = 1.022\,\mathrm{MeV}$), the effects of pair production become visible. The produced electron-positron pair can annihilate and produce two gamma rays with an energy of $m_ec^2 = 0.511\,\mathrm{MeV}$. For a small detector, it is likely that both gamma rays will escape. This results in a so called double escape peak (see Figure 5b) located $1.022\,\mathrm{MeV}$ lower than the full-energy peak. For somewhat larger detectors, it is also possible that only one $0.511\,\mathrm{MeV}$ gamma ray escapes. This results in a single escape peak, located $0.511\,\mathrm{MeV}$ lower than the full-energy peak.
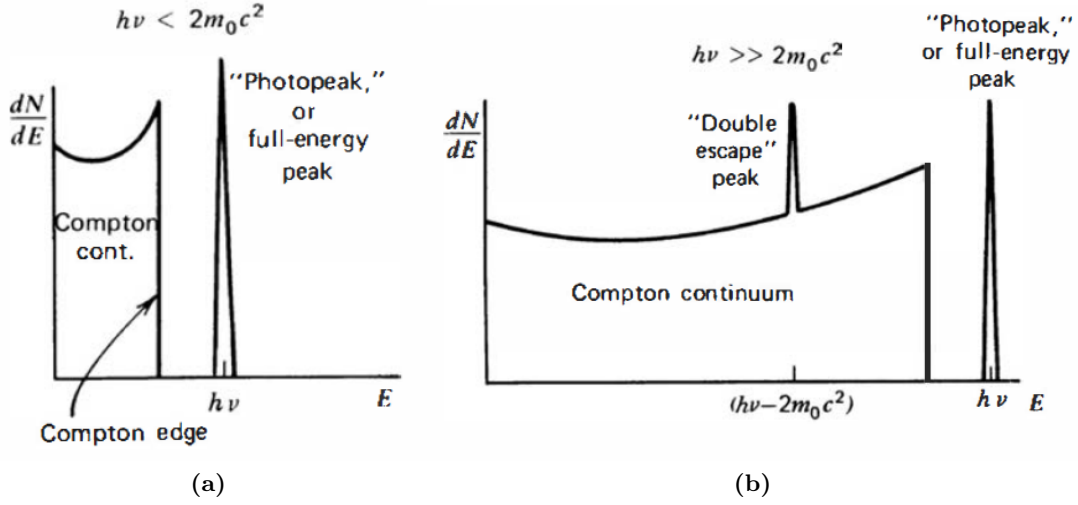
Figure 5: *Two spectra for a small detector: (a) Spectrum for low gamma-ray energies showing the full-energy peak, Compton continuum and Compton edge. (b) A spectrum for higher gamma-ray energies ($> 2m_e c^2$) which also shows the double escape peak. [5]*

The shape of the pulse-height spectrum can also be influenced by surrounding materials. This results in the following possibly visible peaks, which are also made visible in Figure 6.

1. X-ray peaks. The incoming gamma ray can also interact through photoelectric absorption with the shielding material. This in turn can lead to the creation of characteristic x-rays. In the case of lead, which is often used for shielding purposes, these characteristic energies are in the 72 keV to 84 keV range.

2. Backscatter peak. When gamma rays enter surrounding materials, they can be backscattered into the detector. The location of this peak is around 200 keV at the energy of the full-energy peak minus the Compton edge.

3. Annihilation peak. In the case of high energies, pair production in the surrounding material can result in 0.511 MeV photons which can be picked up by the detector.

(a)

(b)

Figure 6: *(a) The processes in a surrounding material which can create additional peaks. (b) The peaks made visible in a pulse-height spectrum. [5]*

2.6.4 Activity calculation

Due to the fact that part of the radiation passes through the detector without interaction and because, in general a detector only has a limited surface area, a detector will not measure all emitted gamma rays. The fraction of gamma rays from the source that is detected, is defined by the detector efficiency ε. Furthermore, a detector will have some dead time. This is the time when no gamma rays can be counted until the system is recovered, which allows for detection of separate events. The dead time δ is defined as:

$$\delta = 1 - \frac{\text{live time}}{\text{real time}} \tag{13}$$

where the live time is the time where the system was able to detect and the real time is the actual passed time. Finally, we take into account there is only a certain probability a radionuclide will emit a gamma ray called the branching ratio f. Using

15

these quantities one can derive an equation which relates the detected number of counts, N_{det}, to the actual number of radionuclides, N, which would have decayed.

$$N_{det} = \varepsilon f (1 - \delta) N \tag{14}$$

By using Equation 8, N can be written in terms of the number of radionuclides present at the start of the measurement, N_m. This gives:

$$N_{det} = \varepsilon f (1 - \delta) N_m \left(1 - e^{-\lambda t_m} \right) \tag{15}$$

where t_m is the measurement time. By again using Equation 8, N_m can be written in terms of the number of radionuclides present right after irradiation, $N(t)$, assuming there is a delay time, t_d, between the irradiation and the measurement. This gives:

$$N_{det}(t; t_m, t_d) = \varepsilon f (1 - \delta) N(t) \left(e^{-\lambda t_d} - e^{-\lambda(t_d + t_m)} \right) \tag{16}$$

We can then realize $N(t)$ is the net number of produced radionuclides after an irradiation time t as was given in Equation 10. With Equation 16 and Equation 11 it is thus possible to determine the activity of a radionuclide right after irradiation through:

$$A = \frac{\lambda N_{det}}{\varepsilon (1 - \delta) f \left(e^{-\lambda t_d} - e^{-\lambda(t_d + t_m)} \right)} \tag{17}$$

Of course this equation can also be used to determine the number of radionuclides at any given time before a measurement.

2.6.5   Minimal detectable activity

If a detector does not measure any activity in an object, it does not necessarily mean the object contains no activity. It might simply be that the number of counts is too low to be distinguished from the background. The so called minimal detectable activity (MDA) gives the lower limit of what activity can be measured. It can be calculated from the number of counts in a peak that can still be distinguished from the background. This number of counts, or detection limit L_D, can be approximated by [22]:

$$L_D = 5.4 + 3.3 \sqrt{2 N_b} \tag{18}$$

where N_b is the number of counts in the background in the same region as where the photopeak of a radionuclide is expected. From this detection limit, the MDA can be calculated by using Equation 17.

2.7   Radiation safety

Using gamma spectroscopy it is possible to determine the activity of a radioactive source in units of becquerel. This indicates the strength of a source but not necessarily the dangers of it. Ionizing radiation deposits energy into living tissues and it is the absorption of this energy that is a potential hazard.

The radiation dose, or absorbed dose, indicated by D refers to the quantity of radiation energy deposited into any substance. It has units of gray (Gy), which equals the deposition of 1 joule per kg of absorbing material. It depends on the source's strength

and geometry, distance to the source, type of radiation and the dose receiving substance[23, 24]. Next to absorbed dose, there is the equivalent dose, H_T, for a type of tissue or organ, T, given in sievert (Sv). This quantity takes into account the biological damage caused by radiation. It depends on the type of radiation. For example, an α-particle has a very local energy deposition whereas a gamma ray deposits its energy over a wider area. A weighting factor, w_R, takes into account these differences. It relates the absorbed dose for a tissue or organ, T, with the equivalent dose with the following equation:

$$H_T = D_T \times w_R \tag{19}$$

For example, for x-rays, gamma rays, electrons and positrons the weighting factor is simply 1. For protons it is 2 and for α-particles it is 20. The weighted sum of the equivalent doses over all tissues in a human body gives the effective dose, E:

$$E = \sum_T w_T H_T \tag{20}$$

where w_T is a tissue weighting factor. The effective dose, also given in units of sievert, represents the risk of all the stochastic effects for an irradiated individual.

The book of Keverling Buisman[25] provides some useful data to calculate the effective dose received by internal contamination (ingestion, inhalation). So called $e(50)$ coefficients in $\mathrm{Sv\,Bq}^{-1}$ are given for both ingestion and inhalation. Multiplication with the source activity gives the total effective dose $E(50)$ over a time period of 50 years. This includes the effects on all tissues or organs. Inhalation coefficients can depend on the lung clearance index, which indicates the time spent in the lungs. However, for ^{7}Be the coefficients are roughly equal for both given classes (Slow and Moderate). The following table lists the coefficients for ^{7}Be:

Table 2: *Dose coefficients for ^7Be in* $\mathrm{Sv\,Bq}^{-1}$

Nuclide	$e(50)$ (ingestion)	$e(50)$ (inhalation)
^{7}Be	2.8×10^{-11}	$4.3\text{-}4.6 \times 10^{-11}$

Since radioactive materials can thus pose a threat, there are regulations which describe how much activity a material may contain. In the Netherlands the "Besluit basisveiligheidsnormen stralingsbescherming"[26] describes these regulations. It contains so called "vrijstellingswaarden", which in this thesis will be called exemption values, and "vrijgavewaarden", which will be called clearance values. If the total activity and activity concentration are below the exemption values, one is allowed to posses and use the material without having a permit. If the activity concentration is below the clearance value, one is allowed to dispose of the material. Depending on the total weight, different values have to be used. Figure 7 shows visually which values have to be used and Table 3 gives these values for relevant nuclides.

Figure 7: *An illustration that describes which values have to be used from Table 3*

Table 3: *Exemption and clearance values for relevant radionuclides[26]*

Nuclide	Column A	Column B	Column C
^{7}Be	$10\,\mathrm{Bq\,g^{-1}}$	$1 \times 10^{3}\,\mathrm{Bq\,g^{-1}}$	$1 \times 10^{7}\,\mathrm{Bq}$
^{54}Mn	$0.1\,\mathrm{Bq\,g^{-1}}$	$1 \times 10^{1}\,\mathrm{Bq\,g^{-1}}$	$1 \times 10^{6}\,\mathrm{Bq}$
^{124}Sb	$1\,\mathrm{Bq\,g^{-1}}$	$1 \times 10^{1}\,\mathrm{Bq\,g^{-1}}$	$1 \times 10^{6}\,\mathrm{Bq}$
^{51}Cr	$100\,\mathrm{Bq\,g^{-1}}$	$1 \times 10^{3}\,\mathrm{Bq\,g^{-1}}$	$1 \times 10^{7}\,\mathrm{Bq}$
^{60}Co	$0.1\,\mathrm{Bq\,g^{-1}}$	$1 \times 10^{1}\,\mathrm{Bq\,g^{-1}}$	$1 \times 10^{4}\,\mathrm{Bq}$

2.8   Estimate of the Be-7 production in air

Before striking a target, the proton beam created by the AGOR cyclotron first passes through roughly 3.5 m of air. Since ^{7}Be can be formed by protons reacting with the nitrogen, oxygen and carbon atoms in air, it is relevant to know how much ^{7}Be can be formed in this 3.5 m. By using Equation 5, the number of produced ^{7}Be atoms from air can be estimated. However, since the cross section appearing in this equation is energy dependent, it is first necessary to know the energy of the proton beam during its passage through 3.5 m of air. The energy of the protons produced by the AGOR cyclotron is in the range of 150 - 190 MeV. Using the Bethe equation (Equation 1), the stopping power in air can be determined and an idea of the energy along the 3.5 m can be obtained. The next paragraphs describe this calculation.

First the the electron density of air has to be determined. This is done using the data from Table 4. Here only the 4 most common elements found in air are listed. These comprise more than 99% of air. Other elements can therefore safely be neglected. Furthermore, it is assumed the air is dry. If an element has a certain fraction of weight in air, then dividing this fraction by the atomic weight M of the element gives the number of moles of per gram of air. Then multiplying with the constant of Avogadro[2] and dividing by the density of air[3] gives the number of particles of the element per cubic meter, i.e. the number density n of atoms. These are listed in the fourth column of Table 4. Finally multiplying with the number of electrons per atom gives the electron density n_e for the element. Summing over all 4 elements gives the total electron density of air: $n_e = 3.62 \times 10^{26}\,\mathrm{m^{-3}}$.

---

[2]   Avogadro constant, $N_A = 6.022\,140\,76 \times 10^{23}\,\mathrm{mol^{-1}}$ [27]
[3]   Density of said air composition $= 1.204\,79 \times 10^{-3}\,\mathrm{g/cm^{3}}$[28]

Table 4: *Composition of air and information regarding its contents.*

Element	weight fraction [28]	M (g/mol) [29]	n (m^{-3})
Carbon (6)	0.000124	12.01	7.49×10^{21}
Nitrogen (7)	0.755267	14.01	3.91×10^{25}
Oxygen (8)	0.231781	16.00	1.05×10^{25}
Argon (18)	0.012827	39.88	2.33×10^{23}

Furthermore, the mean excitation energy of said air composition is $85.700\,\text{eV}$[28]. The last unknown in the Bethe equation is the relative velocity β of the protons. It can be obtained by the following two equations given by Turner [6]:

$$T = E_{total} - E_{rest} = mc^2(\gamma - 1) \tag{21}$$

where for a proton $mc^2 = 938.272\,\text{MeV}$ [27], T is the kinetic energy (150 - 190 MeV), and γ is the relativistic factor given by:

$$\gamma^2 = 1/(1 - \beta^2) \tag{22}$$

From Equation 21, γ is calculated to be 1.16 for 150 MeV and 1.20 for 190 MeV. Using these values in Equation 22, β^2 was calculated to be 0.257 for 150 MeV and 0.308 for 190 MeV. Inserting these values for β, n_e and I, together with the constants[4] m_e, c, e and ϵ_0 in Equation 1 gives the stopping power: $S = 0.580\,\text{MeV/m}$ for 150 MeV and $0.495\,\text{MeV/m}$ for 190 MeV.

For a length of 3.5 m, the lost energy would thus be almost negligible compared to the starting energy. More important, as can be seen in Figure 3, the cross sections for O, N and C are almost constant above an energy of 100 MeV. This means that during the entire 3.5 m in air, the cross sections can, in first order, be estimated as constant and Equation 5 can safely be used to determine the ^{7}Be production rate. From Figure 3 the cross sections for ^{7}Be-production from O, N and C are estimated to be 7 mb, 10 mb and 13 mb, respectively. The number density of the atoms exposed to the beam was given in Table 4. Lastly, the number of incoming protons can be determined by the current of the accelerator as was done in Equation 6.

Applying this information in Equation 5 and summing over all elements gives the production rate of ^{7}Be atoms:

$$R_T = \phi(N_N\sigma_N + N_C\sigma_C + N_O\sigma_O) \tag{23}$$

Inserting all the values then results in 1.0×10^6 ^{7}Be-atoms created per nA per second or $3.7 \times 10^9\,\text{nA}^{-1}\,\text{hour}^{-1}$. This gives an activity of $550\,\text{Bq/nAh}$. The produced activity will be distributed over the whole room. It is likely that ^{7}Be particles will fall down and become visible in the dust and/or leave the room through, for example, ventilation systems. The ^{7}Be activity in dust will later be determined experimentally.

2.9 Estimate of the Be-7 production in PE, PC, Nylon and carbon

The following section includes some preparatory work on the expected ^{7}Be activity in the polyethylene (PE), polycarbonate (PC) and nylon samples (see Figure 8). Moreover, it includes a similar calculation on the beam stop, which activity will later be determined experimentally.

---

[4] Values of these constants were obtained from [27]

Figure 8: *The three samples of polyethylene (PE), polycarbonate (PC) and nylon. Each had a thickness of 4 cm.*

The plan was to use a 150 MeV beam which would be slowed down to 60 MeV using 60 mm of aluminium. According to PSTAR[11], the ranges of 60 MeV protons in PE, PC and nylon are 3.08 cm, 2.70 cm and 2.68 cm, respectively. The samples had a thickness of 4 cm, which would thus be sufficient to fully stop the beam. While slowing down, the energy of the protons decreases until they have zero energy left at these ranges. An implication of this is the large change in energy along their path. Hence, the assumption of a constant cross section, as was used for air, is no longer valid. The same problem is encountered when calculating the expected activity in the carbon beam stop. As can be seen in Figure 3, the cross sections for especially carbon and nitrogen have peaks at lower energies. Note that these are even higher than one might see after a quick inspection due to the logarithmic axis.

To still be able to calculate a rather accurate activity, we can integrate over the entire range with an distance dependent cross section. This results in the following equation for the number of produced nuclides P_T based upon Equation 5:

$$P_T = \int_0^R \phi \sum_i N_i \sigma_i(x) dx \qquad (24)$$

Here we integrate over the distance from 0 to the range R. We thus need to know what the energy of protons is after they travelled a certain distance in each sample. Using the graph from Figure 3 it is then possible to obtain the cross section at each distance. For the energy-distance relation we use the PSTAR database. For PE, PC and Nylon the ranges of energies till 60 MeV (in steps of 1 MeV) are used. When subtracting these from the range of 60 MeV protons it is possible to obtain the energy for each distance travelled till the final range. This is also done for carbon[5] for an energy of 150 MeV since it is expected most protons hitting the beam stop are of that energy.

---

[5] In PSTAR, graphite with a density of 1.7 g/cm^3 was chosen. This was the closest to the 1.8 g/cm^3 carbon used in the beam stop.

The following graphs are then obtained showing the energy for each distance traveled. The interpolation function of Mathematica[30] was used to obtain values between the data points.
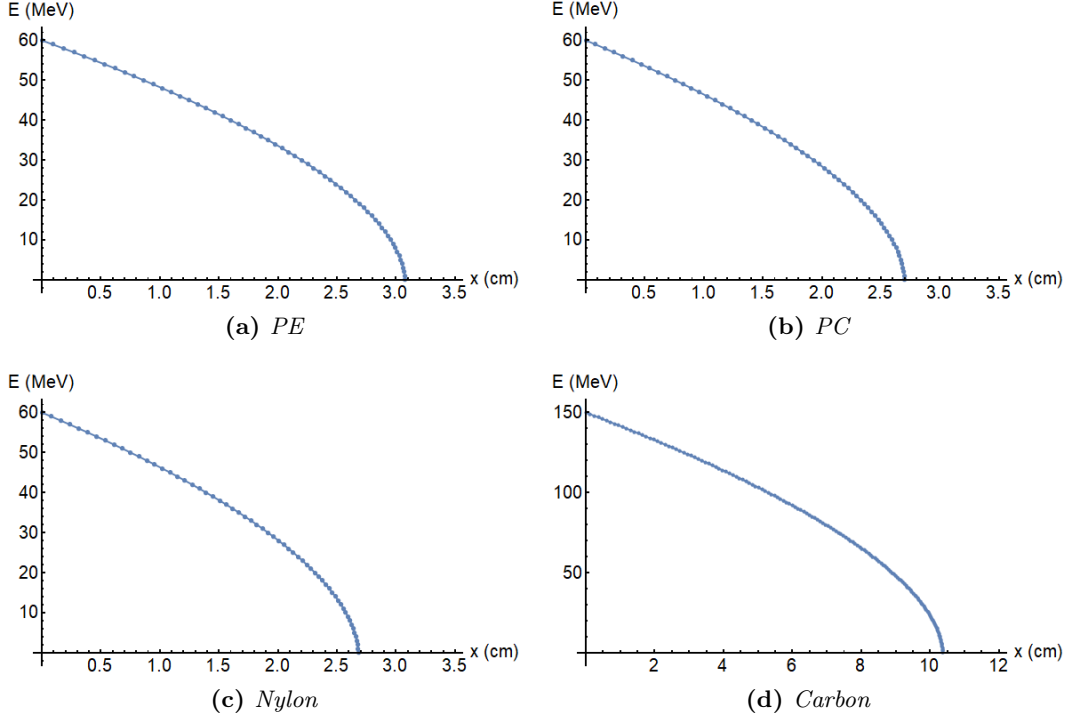
Figure 9: *Figures (a) through (d) show the proton energy as a function of distance traveled in the samples.*

The cross-sectional data from Figure 3 was only provided as a graph in the source article[15]. Therefore, an online tool called WebPlotDigitizer[31], was used to convert this graph into a table of data. The tool can automatically select points on the graph by looking at the colour. By manual selection it was made sure only the straight lines were used and not the dashed lines associated with α-particles. Mathematica was again used to interpolate between the data points. With the energy known at each distance, a function was made in Mathematica which gives the cross section as a function of the distance.

The last values needed for Equation 24 are the number densities. Information regarding the composition of the samples can be found in Table 5. The last column lists the number density of each species of atom which was calculated with the contents of the table in the same way as was done for air. Note that hydrogen is only listed for completeness; it does not contribute to the production of ^{7}Be.

Table 5: *Composition of PE, PC, Nylon and the beam stop*

Element	Weight fraction [11]	M (g/mol) [29]	N (m^{-3})
Polyethylene (PE)			
C$_2$H$_4$, $\rho = 0.94\,\mathrm{g\,cm^{-3}}$			
H	0.143711	1.01	8.055×10^{22}
C	0.856289	12.01	4.036×10^{22}
Polycarbonate (PC)			
C$_{16}$H$_{14}$O$_3$, $\rho = 1.2\,\mathrm{g\,cm^{-3}}$			
H	0.055491	1.01	3.970×10^{22}
C	0.755751	12.01	4.547×10^{22}
O	0.188758	16.00	8.526×10^{21}
Nylon			
C$_{12}$H$_{22}$N$_\mathrm{N}$O$_2$, $\rho = 1.14\,\mathrm{g\,cm^{-3}}$			
H	0.097976	1.01	6.660×10^{22}
C	0.636856	12.01	3.640×10^{22}
O	0.123779	14.01	6.066×10^{21}
N	0.141389	16.00	6.067×10^{21}
Carbon beam stop			
C, $\rho = 1.7\,\mathrm{g\,cm^{-3}}$			
C	1	12.01	8.524×10^{22}

With the number densities of this table and the cross section function it is possible to integrate over the range. The integrals were calculated numerically in Mathematica. The results are listed in the following table. This calculation does not take into account the fraction of the beam that actually strikes the target. For the experiment it was expected that 70% of the starting protons would hit the targets. A 10 nA current for 0.5 hours would then provide measurable kiloBecquerel activities.

Table 6: *Theoretically determined activities for PE, PC, Nylon and the beam stop*

	Activity in Bq per nAh			
	C	O	N	Total
PE	7100	-	-	7100
PC	7000	270	-	7300
Nylon	5600	190	830	6600
Beam stop	47800	-	-	47800

3 Methods

In the following subsections, the methods used to asses the activity in the potential sources will be described. The general method was to use gamma spectroscopy to obtain the net number of counts in the photopeak of a certain radionuclide. Identification of the peaks was performed using the following resources: the Nucléide - Lara application [32] and the Lund/LBNL Nuclear Data Search [33]. To distinguish from natural background radiation, a web-page by the European Nuclear Society was used[34]. Using the detector efficiency, the activity of the source was then calculated using Equation 17.

## 3.1 Be-7 production in the carbon beam stop

In this part we will look at how an estimate of the activity in the beam stop was determined. Naturally, part of this experiment involved gamma spectroscopy. The preferred detector to use would be the HPGe-detector given its superiority over the small CZT-detector. However, given the large size of the beam stop the small portable CZT-detector was used. First, the distribution of ^{7}Be in the beam stop was assessed by placing the detector on various positions on the beam stop. Ten positions were chosen of which five were at the 'top' of the beam stop and five were at the 'bottom'. By the top, the surface directed towards the incoming proton beam is meant. Of these five positions, one was located at the center of the beam stop and four were around it near the edge at a radius of $8\,\mathrm{cm}$. Figure 10a shows the setup with the detector and Figure 10b shows these positions on the beam stop.
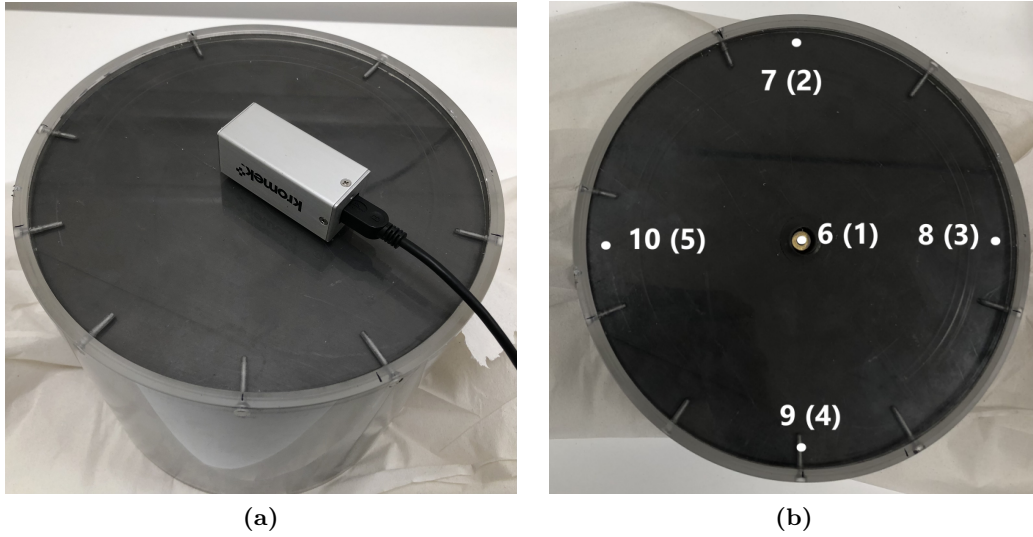
Figure 10: *(a) The measurement setup. (b) A bottom view of the measurement positions on the beam stop. The numbers 6-10 denote the bottom positions and the numbers 1-5 denote the positions on the other side, the top. The bottom side has some small black pen markings on the edges which allow for the identification of the positions on the beam stop.*

Using the provided KSpect software, the net number of counts in the 477.6 keV peak was then measured. In contrast to the software used with the HPGe detector, KSpect does not automatically identify peaks as regions of interest (ROI). Therefore, selecting the peak as a ROI was done manually. The placement of this ROI however, was very sensitive in the following way. Adding or removing one or two channels could sometimes significantly alter into what KSpect would identify as background radiation. To account for this, relatively large uncertainties of 100 - 200 counts were chosen, rather than taking the square root as the uncertainty. All measurements were performed with a live time of 6 hours over the course of roughly one week, which means the results had to be compensated for the decrease in activity during this time.

These measurements only give an idea of the relative distribution of ^{7}Be. The next step is to convert the data provided by these measurements into an estimate of the activity in the beam stop. Since often pencil beams are used, it is unlikely that the ^{7}Be was spread out homogeneously over the whole beam stop. The results also confirmed this was not the case. Therefore, the assumption was made that inside the beam stop an active, cylindrically shaped region was present. Figure 11 shows this schematically. In this active cylinder, the ^{7}Be would then be spread out homogeneously. It was thus the question to determine the depth and radius of the active cylinder which most accurately described the actual ^{7}Be distribution. The key principle used, was that the measurements at all positions on the beam stop must give the same activity. To calculate this activity, it was necessary to know the efficiency of the CZT detector at all measurement positions. Since these efficiencies were not readily available, they were calculated by using Monte Carlo simulations[35].
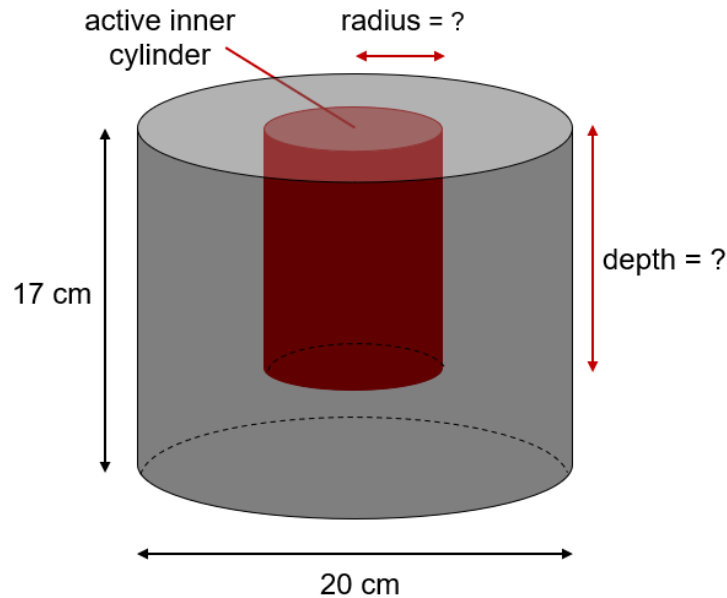
Figure 11: *Schematic overview of an active inner cylinder of unknown size within the beam stop.*

Simulations were performed for different dimensions of the active cylinder. Radii of 20 mm, 40 mm, 60 mm and 80 mm and depths of 62.5 mm, 80 mm, 100 mm and 125 mm were chosen, where the last was based on the average range of 150 MeV and 190 MeV

protons, which are 100 mm and 150 mm, respectively [11]. For all the radii and depths the efficiencies were then calculated for four positions: top centre, top 8 cm, bottom centre and bottom 8 cm. It was thus assumed that the measurements performed at 8 cm will give similar results, due to the source being homogeneous. As turned out, this was a valid assumption. Based on this, the results were averaged. Efficiencies for other depths were obtained through interpolation with Mathematica[30]. Figure 12 shows these for the four positions and radii as a function of depth. It was then possible to use the efficiencies and determine at which depth and radius the activities were equal for the 4 measurement positions and it is that activity which is the total activity of the beam stop.


(a) *Top centre* **(b)** *Top 8 cm*

(c) *Bottom centre* **(d)** *Bottom 8 cm*
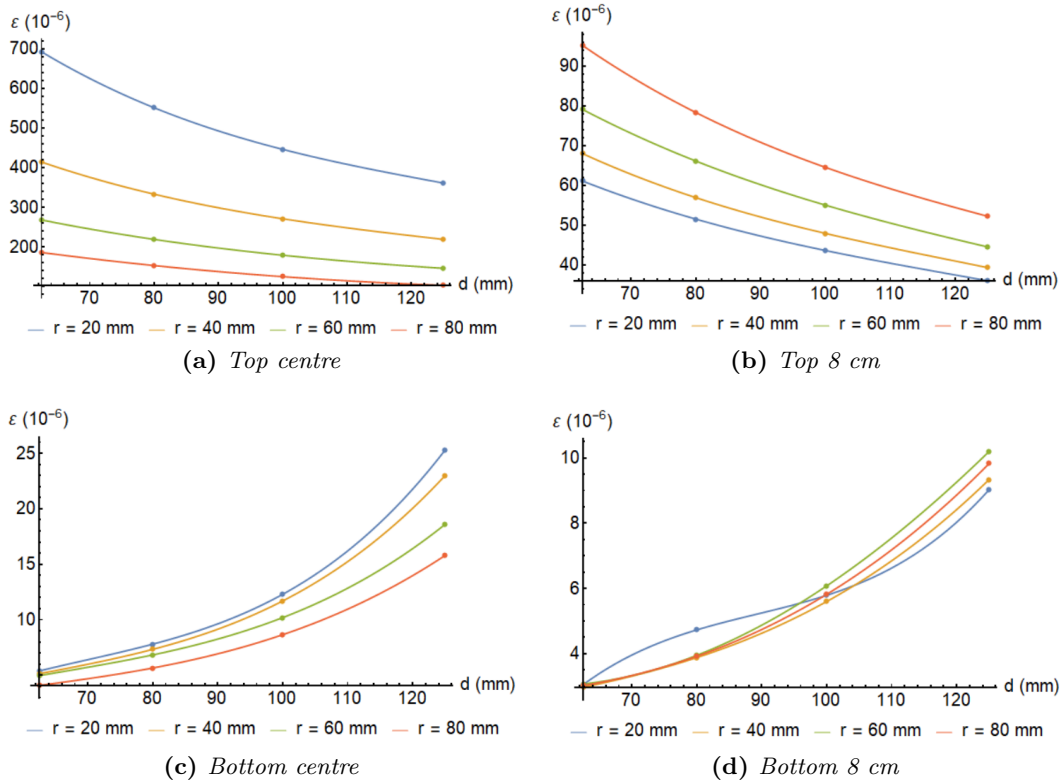
Figure 12: *Figures a through d show the interpolated efficiencies for different radii and measurement positions as a function of depth.*

3.2 Be-7 production in dust

The next part addresses the measurement of ^{7}Be in the dust in the H-cell. Around the beam line in the H-cell, some dust was collected using paper towels. It was collected from the floor and breadboard table. The total area from which dust was collected was roughly $1\,m^2$, but this is just a crude estimate. The paper towels were put in a plastic container which was then placed in the HPGe detector. The sample, shown in Figure 13, was then measured for about 3 days, after which a spectrum was obtained. Compared to the beam stop measurements this is quite a long[6] measuring time. It was expected that the activity in the dust would be very low and that therefore, a

---

[6] About 13 times longer.

long measuring time was needed to obtain detectable results. The contents of this spectrum were then analysed and an estimate of the ⁷Be activity was determined. In contrast with KSpect, the software used with the HPGe detector automatically determines the locations of the peaks and their net contents including uncertainty. Since the HPGe detector was used and the towels were assumed to be similar to filter paper, the efficiency needed for the activity calculation was readily available. Finally, we looked at what would be the effective dose if one were the ingest or inhale such an amount of dust using the $e(50)$ conversion factors from Table 2.
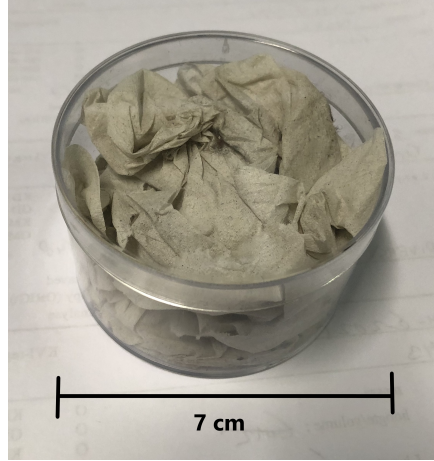

Figure 13: *The dust sample: paper towels in a plastic container with a diameter of* 7 cm *and a height of* 4 cm.

3.3 Radioactivity on the breadboard

Most components along the beam line in the H-cell are mounted on a long L-shaped table with on top a Newport breadboard. As can be seen in Figure 14, the whole table consists of 3 smaller tables, each having dimensions of 1.8 m by 0.9 m. In total the breadboard is 58 mm thick. It consists of three layers: a 3.4 mm thick top layer of stainless steel (400 series), an intermediate polymeric honeycombed layer, and a 3.4 mm bottom layer of carbon steel.

To assess which radionuclides are present in the breadboard, and what their activity is, gamma spectroscopy was again used. Since the measurements had to be performed on location, the Kromek CZT detector was chosen. Placed on the breadboard are various components, which may produce more or less neutrons depending on the component's size, material and function. Therefore, it cannot be assumed that the activity is equal along the breadboard. Because of this, measurements were performed at three locations which are shown in Figure 14. One measurement was performed at the location of the target (0 mm), one at 1300 mm towards the beam entry, and the last one at 2600 mm. To prevent interference from radioactive components on the breadboard, the setup was shielded (excluding bottom) with 10 cm of lead as can be seen in Figure 15.
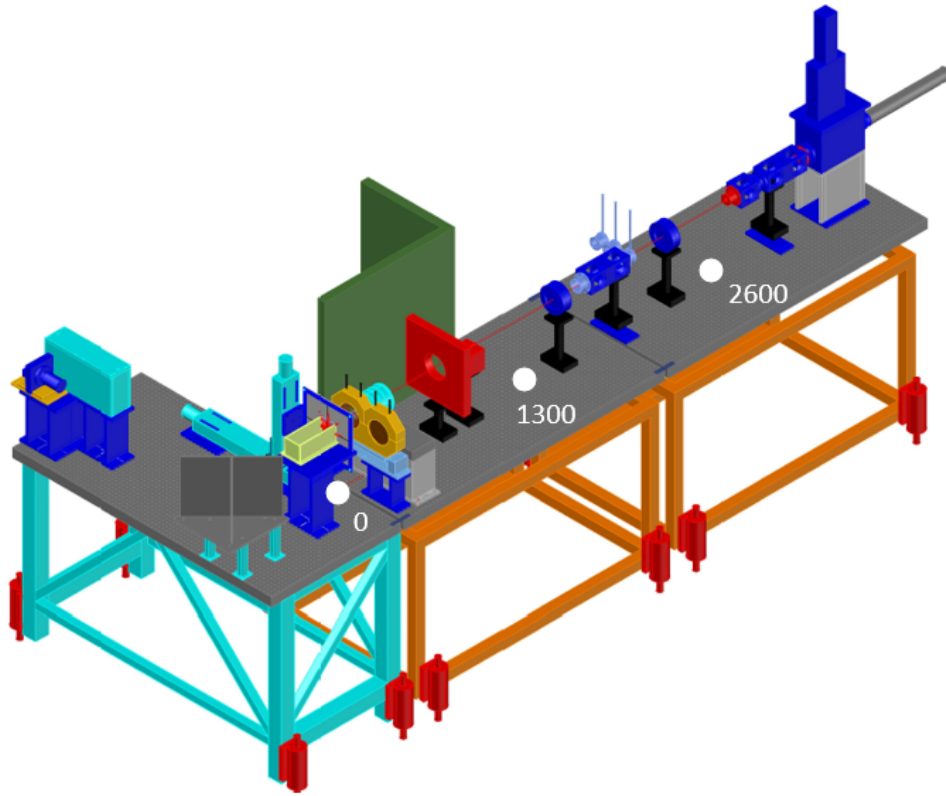
Figure 14: *The three measurement positions. Adapted from [3].*
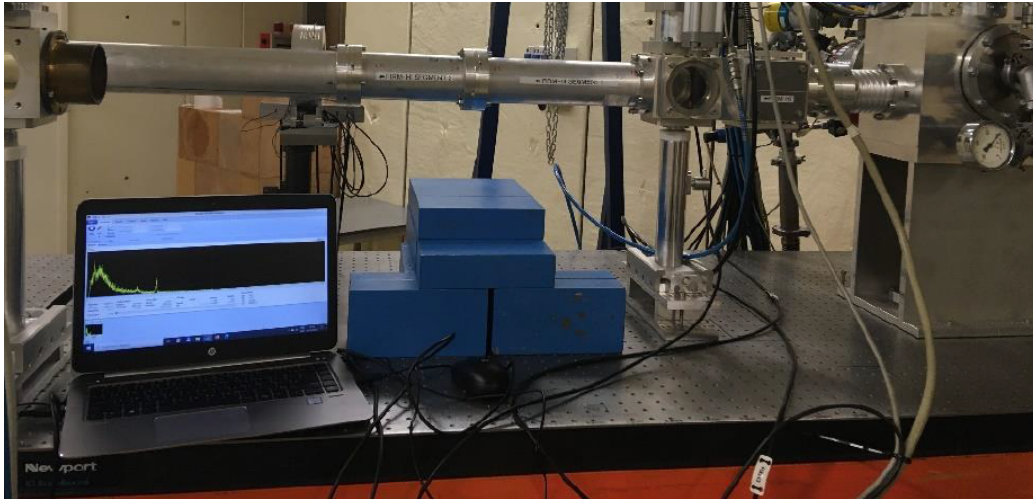
Figure 15: *The setup containing the Kromek CZT detector connected to a laptop. The blue structure is the lead shielding of* 10 cm *thick.* [35]

A measurement was performed for about 3 days for every position. Since one position was measured at a time, the results had to be time compensated, similar to the beam stop measurements. The obtained spectra were then analysed and the activity of the found radionuclides was determined. Determining the contents of the peaks was done similarly to the beam stop measurements by manually creating ROI's. It is relevant

to note that the lead bricks are always located in the H-cell. Therefore it is likely that these bricks also emit some radiation since thermal neutrons could have interacted with them. To separate the gamma rays originating from the lead from the gamma rays originating from the breadboard, a separate measurement on the lead outside the H-cell was performed. For this measurement the detector was fully surrounded (including bottom) with 5 cm of lead. This ensured only gamma rays from the lead were detected.

The efficiencies needed for the activity calculations were again derived using Monte Carlo simulations[35]. In these simulations only the top layer of steel was included. The steel was modelled as a 23.5 by 40 cm plate consisting of 12% Cr and 88% Fe by mass. A density of 7.5 g/cm^3 was taken. The calculated efficiencies were found to follow the following five-parameter rational function:

$$f(x) = \frac{a + bx + cx^2}{1 + dx + ex^2} \qquad (25)$$

where x is the energy in MeV and the parameters have the following values: $a = 8.01 \cdot 10^{-5}$; $b = 8.192 \cdot 10^{-4}$; $c = -1.362 \cdot 10^{-4}$; $d = -9.200$; $e = 42.029$. This function is valid for energies between 0.1 and 3.0 MeV.

Efficiencies for the separate lead measurement were also obtained by Monte Carlo simulations. The following table lists them for the energies of the four most intense gamma rays of ^{124}Sb[35].

Table 7: *Efficiencies for ^{124}Sb.*

Energy (keV)	Efficiency (ε)	Uncertainty
602.73	1.27×10^{-5}	1.6%
645.85	1.19×10^{-5}	1.7%
722.79	1.13×10^{-5}	1.7%
1690.97	5.34×10^{-6}	3.3%

3.4 Radioactivity in the magnets

To identify whether some induced activity was present in the two magnets, measurements were performed inside both magnets. For the 1025 kg magnet, one additional measurement was performed on the outside of it. The measurement positions are marked in Figure 16. For the measurements, the Kromek CZT detector was again used. Due to the expected low activity, rather long measurement times were again chosen of 2 to 4 days. As turned out however, there was no activity visible other than natural background radiation. In the discussion, the minimal detectable activities for ^{54}Mn and ^{60}Co are determined to assess whether any non-detectable activity is below the corresponding clearance values.
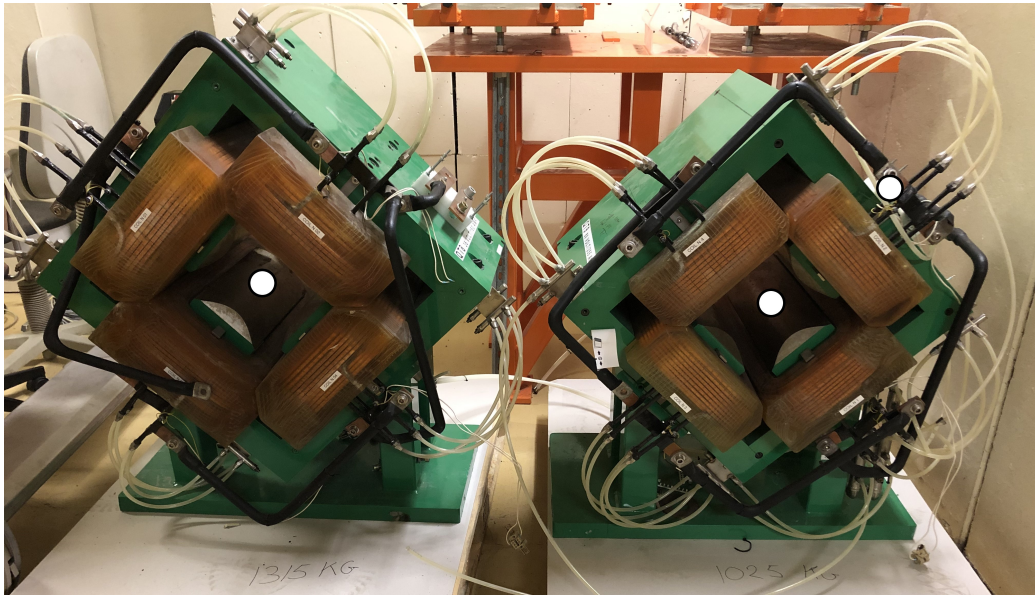
Figure 16: *Left the* 1315 kg *magnet and right the* 1025 kg *magnet. Measurement positions are indicated with the white dots.*

4 Results

4.1 Be-7 production in the carbon beam stop

Each measurement with the Kromek CZT detector gave a spectrum similar to the one seen in Figure 17. For all spectra the 477.6 keV-peak from [7]Be was visible. Furthermore, the 511 keV-peak was visible, which can be attributed to electron-positron annihilation, in part due to background radiation and in part due to beta-plus decay of [22]Na. Next, the backscatter peak is visible around 172 keV and to the right of it is the Compton edge at 304 keV. As was stated in the theory, the sum of these two energies should equal the energy of the photopeak of [7]Be. Summing would give 476 keV which is indeed roughly equal to 477.6 keV. Lastly, in the spectra recorded at the top, a peak located around 1275 keV was visible. A likely source would be [22]Na. It has a lifetime of 2.6 years and decays to stable [22]Ne while emitting a positron and a gamma ray of 1274.5 keV[33]. This radioactive [22]Na is likely the result of proton induced spallation reactions on the thin aluminium foil which is placed only at the top of the beam stop[36]. This would also explain why this peak is not visible on the spectra recorded at the bottom. At log scale there were some minor peaks visible for high energies, located further to the right, which could all be attributed to natural background radiation.
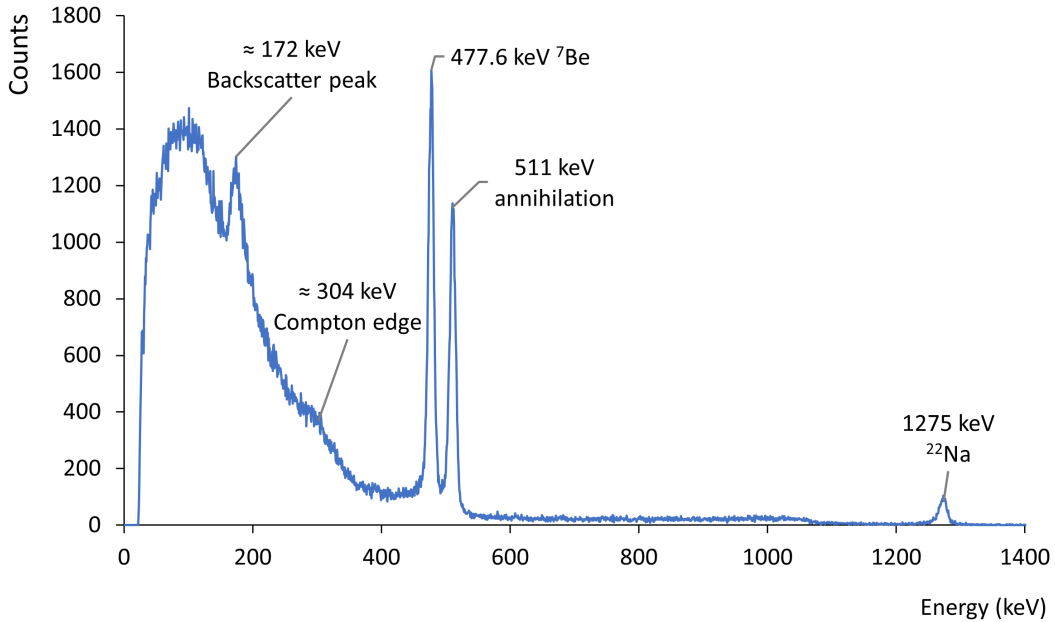
Figure 17: *Example of one the measured spectra for the carbon beam stop. Shown is the spectra at position 1, i.e. the centre at the top.*

We will now focus on the [7]Be peaks. The results for the measurements are given in Table 8. The second column denotes the positions as seen in Figure 10b and the third denotes the time, t_d, at which the measurement was performed relative to the first measurement. For each position the net number of detected counts N_{det} in the 477.6 keV peak in a time period of 6 hours of live time are given in the fourth column. These values came directly from the KSpect software.

We then use Equation 17. This equation includes the required time correction mentioned earlier. The correction factor for dead time was neglected since dead time effects were very small. This was due to the low counting rates which made that the differences between the live and real time were very small (max 4 seconds for 6 hours). We can thus rewrite this equation into:

$$A\varepsilon = \frac{\lambda N_{det}}{f\left(e^{-\lambda t_d} - e^{-\lambda(t_d + t_m)}\right)} \tag{26}$$

The obtained values for $A\varepsilon$ can be found in the last column of Table 8.

**Table 8:** *Number of counts in the Be-7 477.6 keV peak within 6 hours*

	Position	t_d (s)	N_{det} ($\times 10^3$)	$A\varepsilon$ (Bq)
Top	1	0	21(1)	9.5(5)
	2	63900	8.8(5)	4.0(3)
	3	172600	7.7(5)	3.5(3)
	4	409600	7.9(5)	3.7(3)
	5	150300	8.0(5)	3.7(3)
Bottom	6	433500	1.0(1)	0.48(5)
	7	582200	0.6(1)	0.29(5)
	8	604000	0.5(1)	0.26(5)
	9	690000	0.5(1)	0.27(5)
	10	668400	0.5(1)	0.26(5)

As can be seen, the values for the measurements at 8 cm are all roughly equal, most certainly when including the large uncertainties, thus validating the assumption used for the Monte Carlo simulations. If we then average positions 2 to 5 and 7 to 10, the results can be summarized in the following table:

Table 9: *Average $A\varepsilon$ for the beam stop measurements*

	Top centre	Top 8 cm	Bottom centre	Bottom 8 cm
$A\varepsilon$ (Bq)	9.5(5)	3.7(2)	0.48(5)	0.27(3)

Next, the efficiencies obtained from the Monte Carlo simulations were used to obtain the activity. First, the four depths of 62.5 mm, 80 mm, 100 mm and 125 mm were chosen and for each depth a graph was made showing the activity as a function of the radius. Mathematica was again used to obtain the interpolated data for radii other than 20 mm, 40 mm, 60 mm and 80 mm.

(a) $d = 62.5\,\mathrm{mm}$

(b) $d = 80\,\mathrm{mm}$

(c) $d = 100\,\mathrm{mm}$

(d) $d = 125\,\mathrm{mm}$
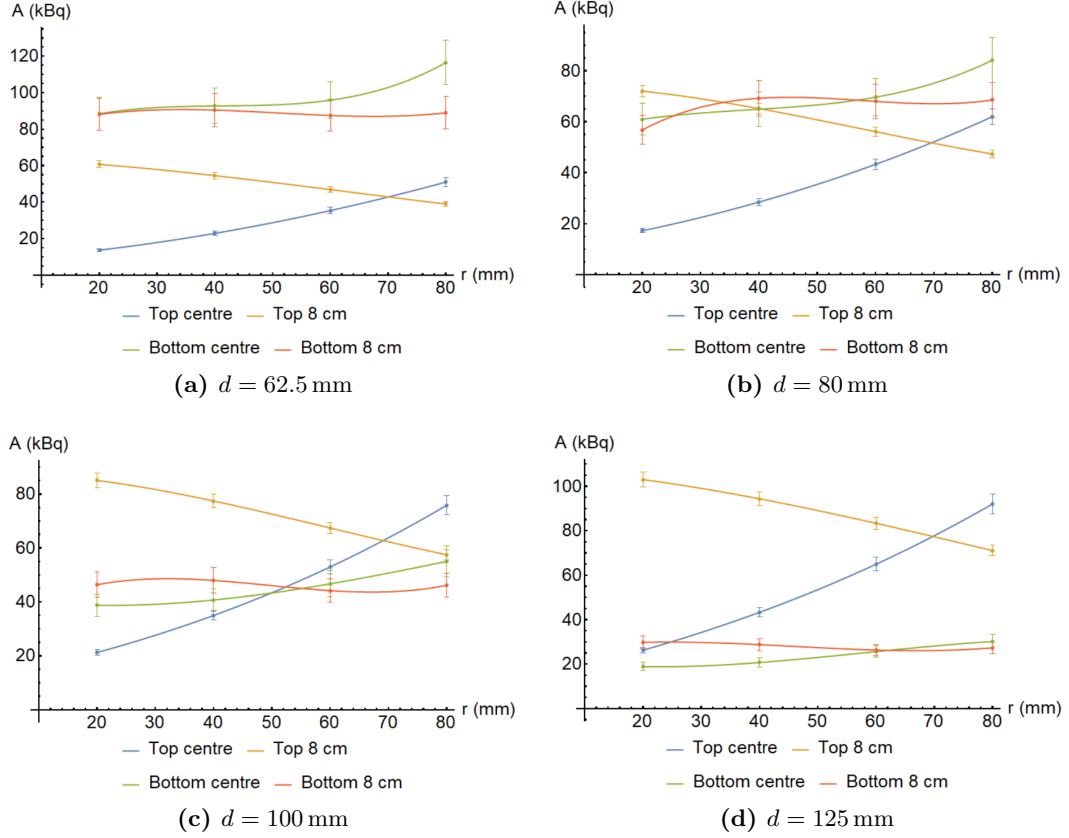
Figure 18: *Figures (a) through (d) show the interpolated activities for the four measurement positions and depths as a function of the radius.*

We know that the activity of the active cylinder should be the same, no matter what measurement position is chosen. Ideally, the lines for all positions should thus coincide at a certain point. From Figure 18 it can be seen that the top positions coincide for all depths at a radius of $70\,\mathrm{mm}$. Based upon this figure, it appears the bottom lines will cross with the top lines somewhere between a depth of $80\,\mathrm{mm}$ and $100\,\mathrm{mm}$. Using the for depth interpolated efficiencies from Figure 12, graphs were made for depths between $80\,\mathrm{mm}$ and $100\,\mathrm{mm}$. Eventually a depth of $90.5\,\mathrm{mm}$ provided the best results as can be seen in Figure 19. The lines do not perfectly cross at the same point, but taking into account the large uncertainties, especially for the bottom lines, a radius of $7(1)\,\mathrm{cm}$ and a depth of $9(1)\,\mathrm{cm}$ seemed most likely as the dimensions of the active cylinder. Using these, the activity of the active cylinder for all measurement positions was found to be $55(8)\,\mathrm{kBq}$. When taking the radius of $7(1)\,\mathrm{cm}$ and the height of $9(1)\,\mathrm{cm}$, the active cylinder has a volume of $14(5) \times 10^2\,\mathrm{cm}^3$. When again assuming a homogeneous distribution of the $^7\mathrm{Be}$, this gives an activity of $4(2) \times 10^1\,\mathrm{Bq/cm}^3$ or $22(8)\,\mathrm{Bq/g}$.
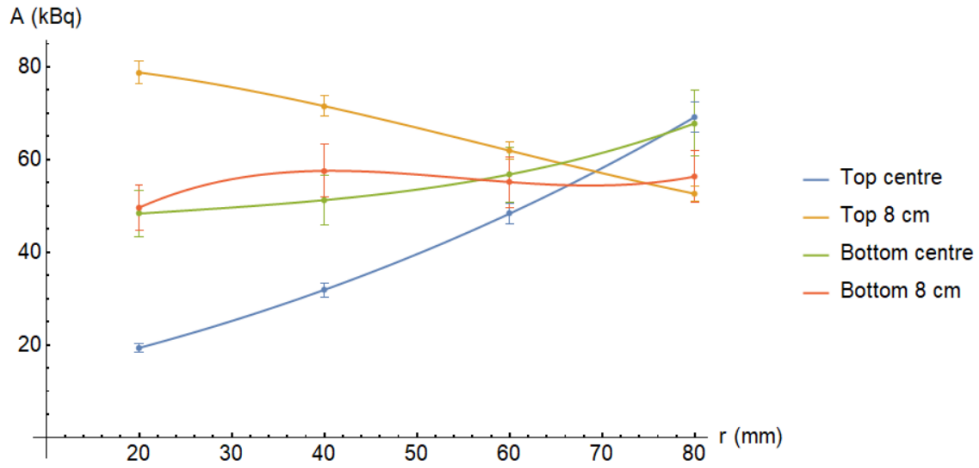
Figure 19: *The interpolated activities for a depth* 90.5 mm *for the four measurement positions.*

4.2 Be-7 production in dust

After examining the dust sample with the HPGe detector, it was found that the only non-natural radionuclide present was ^{7}Be, as can be seen in Figure 20. The measured 478 keV peak contained 1610(62) net counts. Additional peaks were found but these could all be attributed to natural background radiation from ^{40}K and the ^{232}Th and ^{238}U decay chains.
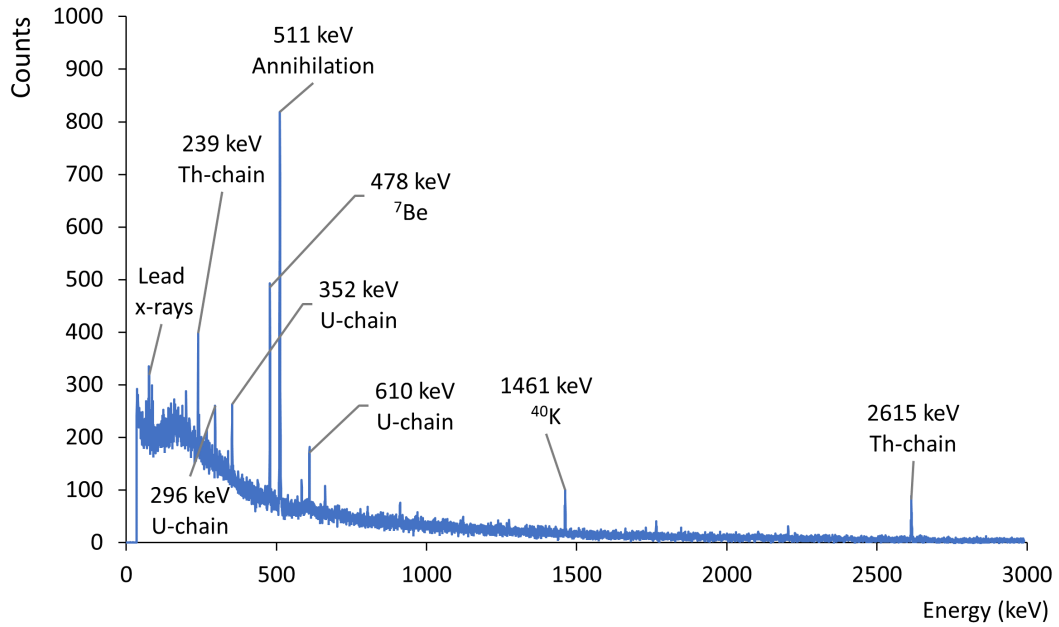
**Figure 20:** *The measured spectrum for the dust measurement.*

Based upon Equation 17, we write that the activity is given by:

$$A = \frac{\lambda N_{det}}{\varepsilon f \left(e^{-\lambda t_d} - e^{-\lambda (t_d + t_m)} \right)} \tag{27}$$

In this equation, dead time effects were again neglected. The measured real time t_m was $232\,054\,\mathrm{s}$ and the live time was $232\,031\,\mathrm{s}$ giving a negligibly small dead time of $\delta = 9.9 \times 10^{-5}$. Finally, the branching ratio f and decay constant λ are again $0.1044(4)$ and $1.507(2)\,\mathrm{s}^{-1}$, respectively. This then gives an activity of the dust sample, at time of measurement ($t_d = 0$), of $0.92(4)\,\mathrm{Bq}$.

4.3 Radioactivity on the breadboard

The measurements at all three positions gave a spectrum such as the one for $2600\,\mathrm{mm}$ which can be seen in Figure 21. The left small peaks at $72\,\mathrm{keV}$ and $84\,\mathrm{keV}$ can be attributed to the lead x-rays. To the right of it is a peak at $320\,\mathrm{keV}$, which can most likely be attributed to the decay of $^{51}\mathrm{Cr}$. The next peak of $511\,\mathrm{keV}$ is due to electron-positron annihilation. The $602\,\mathrm{keV}$ peak is likely due to $^{124}\mathrm{Sb}$. This is further confirmed by the presence of the $1691\,\mathrm{keV}$ peak which should also be visible for $^{124}\mathrm{Sb}$. The largest peak in the spectra is from $^{54}\mathrm{Mn}$ at $835\,\mathrm{KeV}$. Finally, there appear to be some traces of $^{60}\mathrm{Co}$, which can be seen by the $1173\,\mathrm{keV}$ and $1332\,\mathrm{keV}$ peaks. Further on, only the largest peaks ($^{51}\mathrm{Cr}$, $^{124}\mathrm{Sb}$, $^{54}\mathrm{Mn}$) are considered.
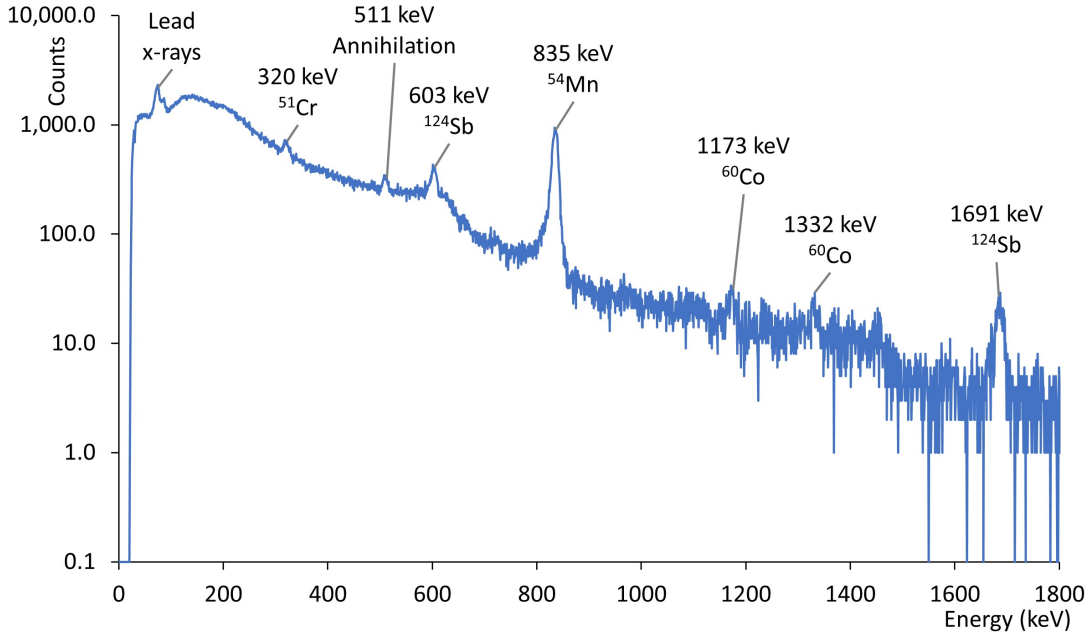
Figure 21: *The measured spectrum at $2600\,\mathrm{mm}$ from the target. The vertical axis is in log scale.*

Table 10 and Table 11 list the measurement times and results of the breadboard measurements. Here t_d is the time delay with respect to the first measurement, t_m is the measurement time and N_{det} is the number of detected counts in the respective peak. Just as before, the dead time effects were negligible. The efficiencies for the respective

energies were calculated with Equation 25. Finally, the activities for all radionuclides were calculated with Equation 27. The measured volume was modelled with dimensions of 23 by 40 by 0.34 cm. Together with the density of the steel ($7.5\,\mathrm{g\,cm^{-1}}$ the activity per gram was calculated. Together with the total activity, these values are given in Table 11.

Table 10: *Measurement times*

Position	t_d (s)	t_m (s)
0 mm	517600	339600
1300 mm	0	246000
2600 mm	246500	270700

Table 11: *Measurement results for the breadboard*

Element	Position	N_{det}	A (Bq)	A ($\mathrm{Bq\,g^{-1}}$)
^{51}Cr	0 mm	$14(2) \times 10^2$	$37(6) \times 10^1$	0.16(2)
	1300 mm	$15(2) \times 10^2$	$46(7) \times 10^1$	0.19(3)
	2600 mm	$23(3) \times 10^2$	$69(9) \times 10^1$	0.29(4)
^{124}Sb	0 mm	$14(2) \times 10^2$	$9(2) \times 10^1$	0.039(6)
	1300 mm	$16(2) \times 10^2$	$14(2) \times 10^1$	0.058(8)
	2600 mm	$33(3) \times 10^2$	$27(3) \times 10^1$	0.11(2)
^{54}Mn	0 mm	$105(5) \times 10^2$	$106(6) \times 10^1$	0.44(2)
	1300 mm	$151(5) \times 10^2$	$208(7) \times 10^1$	0.87(3)
	2600 mm	$190(8) \times 10^2$	$24(2) \times 10^2$	1.00(6)

Note that for the above results, it is assumed the found radionuclides are present in the breadboard. This is due to the efficiencies which were calculated with this assumption. Since ^{124}Sb was also found in lead, as will be discussed in the next paragraph, the calculated activities for ^{124}Sb are likely not correct.

For the lead measurement a spectrum was obtained which only showed peaks which could be attributed to ^{124}Sb as can be seen in Figure 22. The most right peak is also due to ^{124}Sb and has a branching ratio of only 5.5%. The number of counts in this peak is too low to say anything meaningful about it. Besides these peaks there is also a double escape peak of the 1691 keV peak visible at 669 keV. The single escape peak is not visible which can be explained by the fact that we are dealing with a small detector[5]. Finally, some peaks due to the lead x-rays and annihilation can be seen. Next, the net number of counts for the four ^{124}Sb-peaks was determined. The resulting values can be found in Table 12. With these, the activities were calculated. In this calculation, a measurement time of 517800 seconds was taken. Dead time effects were negligible and the efficiencies from Table 7 were used. The obtained activities can be seen in Table 12.
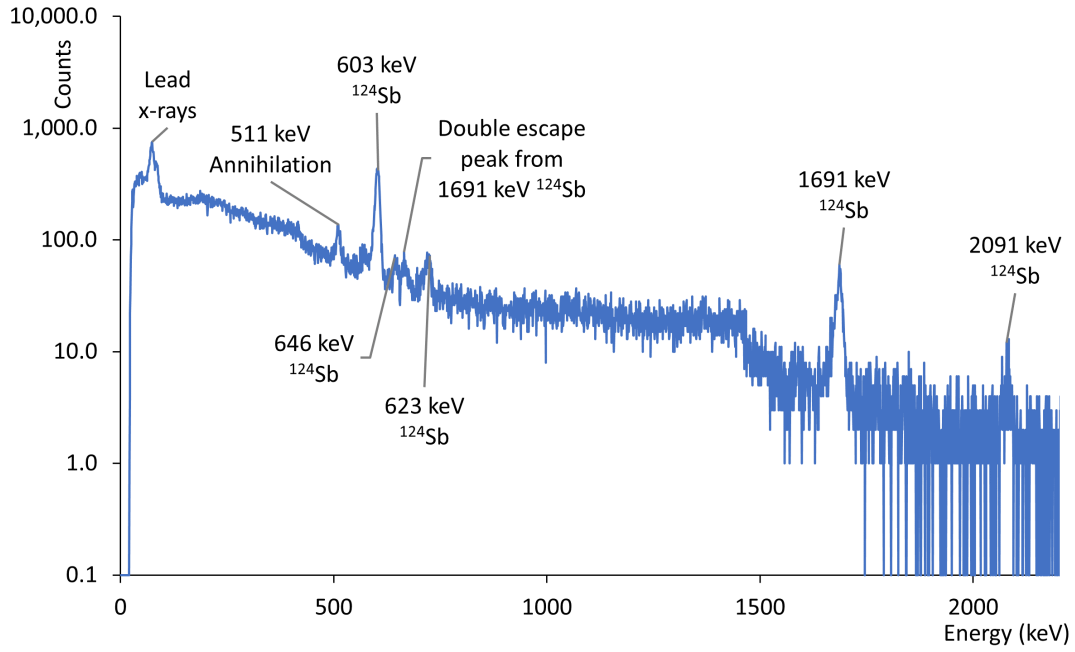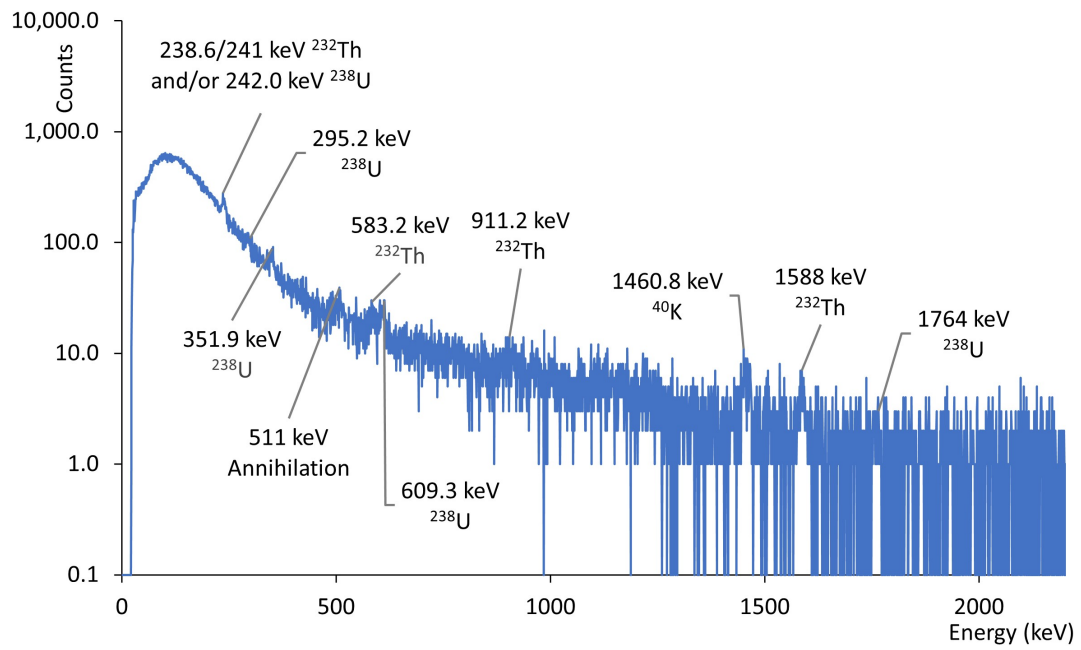
Figure 22: *The measured spectrum for the lead shielding bricks. The vertical axis is in log scale.*

Table 12: *Measurement results for ^{124}Sb in lead.*

Energy (keV)	N_{det}	A (Bq)
602.73	$7.0(5) \times 10^2$	$11.3(9) \times 10^2$
645.85	$5(1) \times 10^2$	$11(3) \times 10^2$
722.79	$7(2) \times 10^2$	$12(3) \times 10^2$
1690.97	$13(2) \times 10^2$	$10(2) \times 10^2$

4.4 Radioactivity in the magnets

All four measurements on the two magnets showed a spectrum similar to the one seen in Figure 23. As can be seen, all peaks could be attributed to background radiation from either ^{40}K or the ^{232}Th and ^{238}U decay chains.

Figure 23: *The measured spectrum for the* 1025 kg *magnet. The vertical axis is in log scale.*

5 Discussion

## 5.1 Be-7 production in the carbon beam stop

The activity density of the active cylinder was $22(8)$ Bq/g. The exemption values for ^{7}Be are 1×10^3 Bq/g or a total activity of 1×10^7 Bq. In the case of the beam stop, the found activity is thus below these values. It is however above the clearance value of 10 Bq/g.

To get an idea of what proton load could have created such an activity, we look back at the theory section. We there found that in the beam stop a 150 MeV beam could create an activity of around $48\,000$ Bq/nAh. This implies a 150 MeV proton load of 1.2 nAh is enough to create such activity.

It is important to note that the obtained activity is the activity at the moment of the first measurement. ^{7}Be has a half life of 53 days and depending on what the experimental history looks like, the activity could have been a factor 2 higher, or even more.

Another important note is that the obtained activity can only be taken as an estimate. If we look at the activity per gram ($22(8)$ Bq/g) the uncertainty is as high as 36%, which in turn results from both the high uncertainty in the total activity and in the estimated volume of the active cylinder. This becomes clear when looking at Figure 19. The lines do not perfectly cross at one point. Especially for the bottom measurements the error bars are large. The foremost reason for this was the difficulty in determining the net number of counts. The number of counts was quite low for these measurements which made distinguishing the peak from the background more difficult. For future experiments, this problem can easily be solved by increasing the measurement time and performing the measurements closer the the last irradiation such that the activity is higher.

Furthermore, there is one assumption that was made that is likely not entirely true: the ^{7}Be concentration was taken as homogeneous. The measurements at 8 cm confirmed the ^{7}Be was spread out quite evenly across the edge of the cylinder. However, because of the nature of the experimental setup, it is impossible to say that the ^{7}Be was spread evenly across the depth. If we look back at the theory section (subsection 2.9) and make a graph of the function we integrated, we see the following:
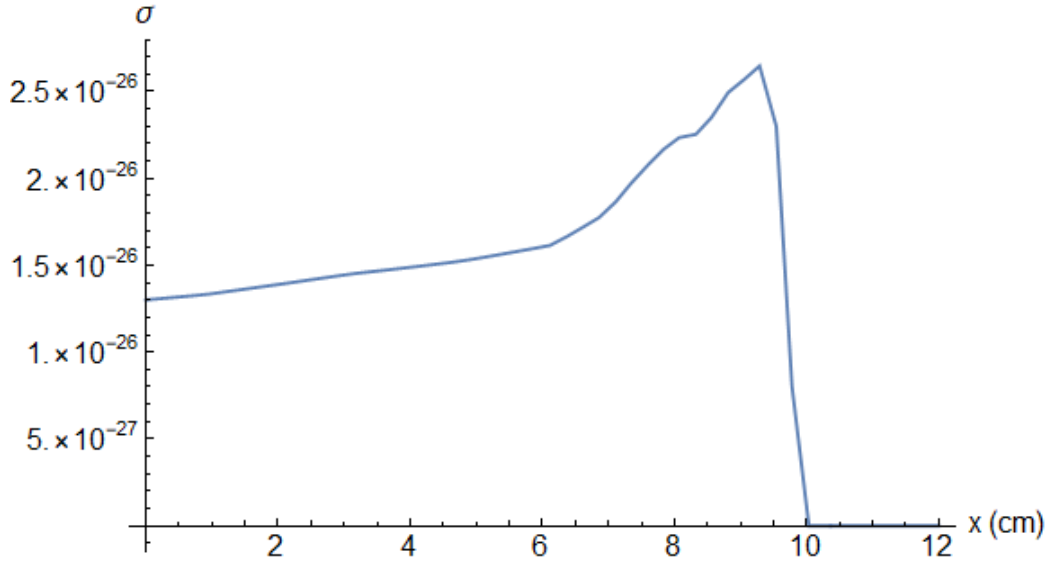
Figure 24: *The cross section of carbon as a function of the distance traveled in the beam stop (*150 MeV *protons)*

It is immediately clear that the top part of the beam stop is expected to have a lower ^{7}Be concentration than the middle part. Thus, the homogeneity assumption is not necessarily true. This emphasizes that the measured activity per gram should only be taken as a rough estimate, since the middle part of the beam stop could have a higher activity than the one determined. Based on the cross sections, the difference between the activities at different locations in the active cylinder should be at most a factor 2. If one were interested in a more accurate determination of the activity distribution, the beam stop could be cut into slabs which could then be measured separately. For an even more accurate measurement some samples could be made which are small enough to be measured in the HPGe detector. This was unfortunately not possible for this experiment since the beam stop was needed again.

In the end, this experiment showed that the beam stop can be roughly treated as having an active cylinder with a radius of 7(1) cm and a height of 9(1) cm, which contains a homogeneous distribution of ^{7}Be. With this information it is now possible to perform a single measurement witht the Kromek detector and with that, estimate the ^{7}Be activity. The preferred location of this measurement is the top centre position, since it gives the highest number of counts. At this position, the activity can thus be calculated with an efficiency of:

$$\varepsilon = \frac{A\varepsilon}{A} = \frac{9.5(5)\,\mathrm{Bq}}{55(8) \times 10^3\,\mathrm{Bq}} = 1.7(3) \times 10^{-4} \tag{28}$$

Where A is the total activity and $A\varepsilon$ is measured value of the top centre measurement from Table 9.

5.2   Be-7 production in dust

The dust measurement gave an activity of 0.92(4) Bq. Since the sample was taken from a surface area of roughly 1 m^2 it can be concluded that the floor and other surfaces are coated with dust having an activity due to ^{7}Be of about 1 Bq/m^2.

To get an idea of the harm this dust sample might do, the $e(50)$ coefficients from Table 2 can be used to calculate the effective dose a person received in 50 years when the sample is ingested or inhaled. This gives a dose of $2.6(1) \times 10^{-5}$ µSv or $4.1(2) \times 10^{-5}$ µSv when ingested or inhaled, respectively. It is however, relevant to note that the measured activity and dose can only be taken as a very crude estimate. The dust was randomly collected from various places around the beam line. It is thus impossible to say whether the concentration of ^{7}Be is constant across the H-cell. Neither can anything be said on how much dust floats around and will thus be inhaled.

What we can do is making a very rough, back of an envelope, estimation of the dose received when working in the H-cell. For this we take some extremities. Let us say we have a person who has to work 8 hours per day in the H-cell. If we assume the extreme case that the person would consume all of the dust on the floor in this day, he would consume $50\,\mathrm{Bq}$ of ^{7}Be activity. The total dose received would then be 1.4×10^{-3} µSv to 2.2×10^{-3} µSv in this day, depending on whether the dust is ingested or inhaled. There is a limit which states that personnel may receive a maximum of $20\,\mathrm{mSv}$ per year, corresponding to $10\,\mathrm{µSv}$ per hour and thus $80\,\mathrm{µSv}$ in a day. Though the total effective dose, which was just calculated, is received during a time period of 50 years, it is attributed to the time when it was received[7], which is 8 hours. When compared to the limit of $80\,\mathrm{µSv}$, 1.4×10^{-3} µSv to 2.2×10^{-3} µSv is about a factor 4×10^4 smaller. It is thus safe to say that the ^{7}Be present in dust poses no threat to working personnel.

5.3 Radioactivity on the breadboard

On the breadboard ^{51}Cr, ^{124}Sb and ^{54}Mn were found, together with some small traces of ^{60}Co. For the latter it was impossible to determine the activity for the peaks were too small for the KSpect software to say anything about the contents of these peaks. Apart from ^{124}Sb, the identified radionuclides could be expected after neutron interactions with steel. Since ^{124}Sb was also found in the separate lead measurement it makes sense for that to originate from the lead castle, instead of the breadboard itself. As far as the author could find, antimony is not used in steel, but only a second measurement with non-exposed lead could prove it truly originates from the lead. This thus means the calculated activities on the breadboard are not valid for antimony.

If we look at the found activities from Table 11, we see a general trend visible: an increasing activity from $0\,\mathrm{mm}$ to $2600\,\mathrm{mm}$. A possible explanation can be found in the components along the beam line. The difficulty herein lies in the fact that, depending on the experiment, different components are placed at different positions. However, typical for the $2600\,\mathrm{mm}$ position is the scatter foil that is often placed near it. It is thus likely that neutrons produced due to this scatter foil are partly responsible for the higher activity.

Though the activities are not correct, this trend of increasing activity is also visible for ^{124}Sb. One explanation might be that the different lead bricks have different activities itself. When assembling and disassembling the lead castle, the bricks were likely mixed. This means that in the $2600\,\mathrm{mm}$ measurement, bricks with a higher activity were likely placed closer to the detector. Another explanation is that ^{124}Sb is

---

[7] According to [26], the total internally received effective dose should be attributed to the year when it was received. Hence, the decisions to assign this dose to the 8 hours.

present in the breadboard, either in the steel or the polymeric middle layer. Again, only a second measurement could tell whether this is the case.

The found activities on the breadboard can also be compared to the exemption and clearance values. For that we look at the total weight. The full breadboard table in the H-cell consists of three, 180 by 90 cm tables. Taking only the top layer with a density of $7.5\,\mathrm{g\,cm^{-3}}$, the total mass of this layer is:

$$m = 300 \times 150 \times 0.34 \times 3 \times 7.5 = 124 \times 10^3\,\mathrm{g} = 124\,\mathrm{kg}$$

Which is well below the $1000\,\mathrm{kg}$ limit. In that case, both the total activities and the activity concentrations are all below the exemption values from column C and B of Table 3. Note that for ^{54}Mn, the activity concentrations are above the clearance value of $0.1\,\mathrm{Bq\,g^{-1}}$ for all three positions. For ^{51}Cr the activity concentration is below the clearance value.

The measurements show that for the steel breadboard, the most important source of gamma radiation is ^{54}Mn which is produced through neutron interactions with iron. It is thus expected that not only the breadboard but also other steel (or iron) structures in the H-cell contain ^{54}Mn in a concentration above the clearance value.

5.4 Radioactivity in the magnets

The magnets showed no activity with the Kromek CZT detector. This does not necessarily mean the magnets do not contain any activity. The activity could be too low to stand out against the background of the spectrum. ^{60}Co and ^{54}Mn are the two elements with long half-lives from which some activity could be expected. Therefore, we determine the minimal detectable activity for these two radionuclides, more specifically, for the $835\,\mathrm{keV}$ peak of ^{54}Mn and the $1173\,\mathrm{keV}$ and $1332\,\mathrm{keV}$ peaks of ^{60}Co.

The average width of the ^{54}Mn peaks of the breadboard spectrum was 65(5) channels. This same width was used to determine the number of counts of the background at the location of the photopeaks in the spectra of the magnets. These numbers are given in Table 13, together with the measuring time, t_m. Using the following equation, derived from Equation 17 and Equation 18 the minimal detectable activity (MDA) was calculated:

$$MDA = \frac{\lambda(5.4 + 3.3\sqrt{2N_b})}{\varepsilon f \left(1 - e^{-\lambda t_m}\right)} \tag{29}$$

Efficiencies for this calculation were obtained from [37]. These were calculated by performing Monte Carlo simulations. For the inner measurements the assumption was made that the Kromek detector was placed at $11.5\,\mathrm{cm}$ above a plate of 23 by 40 by $7\,\mathrm{cm}$, consisting of 50% Cu and 50% Fe with a density of $8.5\,\mathrm{g/cm^3}$. The total weight of the detected volume was thus:

$$23 \times 40 \times 7 \times 8.5 = 54\,740\,\mathrm{g}$$

For the outer measurement the assumption was made that the Kromek detector was placed directly on a plate of 10 by 10 by 7 cm, consisting again of 50% Cu and 50% Fe with a density of $8.5\,\mathrm{g/cm^3}$. The total weight of this volume was:

$$10 \times 10 \times 7 \times 8.5 = 5950\,\mathrm{g}$$

The calculated activities were divided by the weights to obtain values for the MDA in Bq/g. These are shown in Table 13.

Table 13: *Minimal detectable activity of ^{60}Co and ^{54}Mn.*

Measurement	t_m	Element	E (keV)	N_b	MDA (Bq/g)
1025 kg Inside	325600	^{54}Mn	835	520(40)	0.0022(2)
		^{60}Co	1173	310(30)	0.0025(2)
		^{60}Co	1332	170(10)	0.0022(2)
1025 kg Outside	261200	^{54}Mn	835	1370(70)	0.0025(2)
		^{60}Co	1173	840(50)	0.0030(2)
		^{60}Co	1332	330(30)	0.0023(2)
1315 kg Inside	212000	^{54}Mn	835	460(40)	0.0032(2)
		^{60}Co	1173	270(30)	0.0036(2)
		^{60}Co	1332	140(10)	0.0032(2)

Both ^{54}Mn and ^{60}Co have clearance values of 0.1 Bq/g. It is immediately clear from Table 13 that the minimal detectable activities of these radionuclides in the magnets are a factor 30-40 lower, meaning, that using this setup an activity above the clearance value should be detectable. Since no activity was detected, any activity in the magnets due to ^{54}Mn and ^{60}Co is thus below the clearance values.

6 Conclusion

The aim of this thesis was to determine the induced activity in air, dust, the carbon beam stop, and the breadboard in the H-cell and two magnets from the TRIµP beam line. Theoretically, it was determined that an activity due to ^{7}Be of $550\,\text{Bq/nAh}$ is produced in a $3.5\,\text{m}$ column of air for protons with energies higher than $100\,\text{MeV}$. For lower proton energies, the cross sections are higher and a higher activity can thus be expected. Next to this, it was determined that the carbon beam stop can be modelled as having an active cylinder with a radius of $7(1)\,\text{cm}$ and a depth of $9(1)\,\text{cm}$. At time of measurement, the activity due to ^{7}Be of this cylinder was $22(8)\,\text{Bq/g}$. Using this data, it was established that for future experiments a single measurement on the top centre position can be used to determine the activity of the beam stop using an efficiency of $1.7(3) \times 10^{-4}$. In addition, the ^{7}Be activity of a dust sample was determined to be $0.92(4)\,\text{Bq}$. With such an activity it is unlikely that dust floating around the H-cell poses any threat to personnel. The last object investigated in the H-cell was the breadboard. On it ^{54}Mn was found with a maximum activity concentration of $1.00(6)\,\text{Bq/g}$ and ^{51}Cr with a maximum activity concentration of $0.29(4)\,\text{Bq/g}$. Also visible were some ^{60}Co traces and ^{124}Sb. The latter was most likely from the lead shielding used in the experiment. Finally, two large magnets from the TRIµP beam line were investigated. On both the inside and outside no measurable activity was found with the Kromek CZT detector. Determining the minimal detectable activities showed any induced activity due to ^{54}Mn or ^{60}Co should be lower than their respective clearance values.

References

[1] C. Bungau et al., "Induced activation in accelerator components", Physical Review Special Topics - Accelerators and Beams **17** (2014).

[2] "Personal communication with Emiel van der Graaf", 2021.

[3] *AGORFIRM specifications*, (2019) https://www.rug.nl/kvi-cart/research/facilities/agor/agorfirm/agor-specifications?lang=en (visited on 05/24/2021).

[4] R. G. Helmer and E. Schönfeld, *Table de radionucléides: Be-7*, (2004) http://www.lnhb.fr/nuclides/Be-7_tables.pdf (visited on 04/20/2021).

[5] G. F. Knoll, *Radiation detection and measurement*, 3rd ed. (Wiley, Weinheim, DE, 2000).

[6] J. E. Turner, *Atoms, radiation, and radiation protection*, 3rd ed. (Wiley, Weinheim, DE, 2007).

[7] J. Lilley, *Nuclear physics: principles and application*, 1st ed. (Wiley, West Sussex, UK, 2001).

[8] S. R. Cherry, J. A. Sorenson, and M. E. Phelps, "Radiation detectors", in *Physics in nuclear medicine* (Saunders Elsevier, Philadelphia, PA, USA, 2012) Chap. 7.

[9] *Gamma spectroscopy*, https://www.nuclear-power.net/nuclear-engineering/radiation-detection/gamma-spectroscopy/ (visited on 06/08/2021).

[10] *Semiconductor detectors*, https://www.nuclear-power.net/nuclear-engineering/radiation-detection/semiconductor-detectors/ (visited on 06/08/2021).

[11] NIST, *PSTAR*, https://physics.nist.gov/PhysRefData/Star/Text/PSTAR.html (visited on 05/13/2021).

[12] D. Filges and F. Goldenbaum, *Handbook of spallation research*, 1st ed. (Wiley, Weinheim, DE, 2009).

[13] Wikipedia, *Spallation*, https://en.wikipedia.org/wiki/Spallation#/media/File:NuclearReaction.svg (visited on 06/29/2021).

[14] A. H. Sullivan, *A guide to radiation and radioactivity levels near high energy particle accelerators* (Nuclear technology publishing, Ashford, UK, 1992).

[15] V. Tatischeff, B. Kozlovsky, J. Kiener, and R. J. Murphy, "Delayed x- and gamma-ray line emission from solar flare radioactivity", The Astrophysical Journal Supplement Series **165**, 606–617 (2006).

[16] R. G. Helmer and E. Schönfeld, *Table de radionucléides: Cr-51*, (2014) http://www.lnhb.fr/nuclides/Cr-51_tables.pdf (visited on 05/29/2021).

[17] Royal society of chemistry, *Antimony*, https://www.rsc.org/periodic-table/element/51/antimony#:~:text=Antimony%20is%20a%20semi%2Dmetal,improve%20their%20hardness%20and%20strength. (visited on 05/30/2021).

[18] R. G. Helmer and E. Schönfeld, *Table de radionucléides: Sb-124*, (2009) http://www.lnhb.fr/nuclides/Sb-124_tables.pdf (visited on 05/29/2021).

[19] R. G. Helmer and E. Schönfeld, *Table de radionucléides: Mn-54*, (2014) http://www.lnhb.fr/nuclides/Mn-54_tables.pdf (visited on 05/29/2021).

[20] R. G. Helmer, *Table de radionucléides: Co-60*, (2006) http://www.lnhb.fr/nuclides/Co-60_tables.pdf (visited on 05/29/2021).

[21] Kromek, *Kromek GR1*, https://www.kromek.com/product/gr1/ (visited on 05/14/2021).

[22] K. Debertin and R. G. Helmer, *Gamma- and x-ray spectrometry with semiconductor detectors* (North Holland, Amsterdam, NL, 1988).

[23] *Absorbed Dose*, https://www.nuclear-power.net/nuclear-engineering/radiation-protection/absorbed-dose/ (visited on 05/30/2021).

[24] J. E. Martin, "Interactions of radiation with matter", in *Physics for radiation protection*, 3rd ed. (Wiley, Weinheim, DE, 2013) Chap. 7.

[25] A.S. Keverling Buisman, *Handboek radionucliden* (BetaText, Bergen, NL, 1996).

[26] Overheid, *Besluit basisveiligheidsnormen stralingsbescherming*, (2018) https://wetten.overheid.nl/BWBR0040179/2018-07-01 (visited on 05/30/2021).

[27] NIST, *Fundamental physics constants*, (2018) https://physics.nist.gov/cuu/Constants/index.html (visited on 04/17/2021).

[28] NIST, *Composition of air, dry (near sea level)*, https://physics.nist.gov/cgi-bin/Star/compos.pl?ap104 (visited on 04/16/2021).

[29] CIAAW, *Atomic weights of the elements 2019*, (2019) https://ciaaw.org/atomic-weights.htm (visited on 04/16/2021).

[30] *Wolfram Mathematica*, https://www.wolfram.com/mathematica/ (visited on 05/20/2021).

[31] *WebPlotDigitizer*, (2020) https://automeris.io/WebPlotDigitizer/ (visited on 05/14/2021).

[32] Laboratoire National Henri Becquerel, *Nucléide - Lara*, http://www.lnhb.fr/nuclear-data/module-lara/ (visited on 05/30/2021).

[33] S. Chu, L. Ekström, and R. Firestone, *The Lund/LBNL Nuclear Data Search*, (1999) http://nucleardata.nuclear.lu.se/toi/index.asp (visited on 05/11/2021).

[34] European Nuclear Society, *Decay Chains, Natural*, https://www.euronuclear.org/glossary/decay-chains-natural/ (visited on 05/30/2021).

[35] E.R. van der Graaf, "Kromek GR1 gamma ray spectrometer efficiencies for the carbon beam stop and for the Newport breadboard in the H-cell", unpublished, 2021.

[36] V. di Napoli, A. M. Lacerenza, F. Salvetti, H. G. de Carvalho, and J. B. Martins, "Production of na-24 and na-22 from al-27 by high-energy photons", Lett. Nuovo Cimento **1**, 835–838 (1971).

[37] E.R. van der Graaf, "Excel sheet with efficiencies for the magnets from the TRIµP beam line", unpublished, 2021.